Universität Bonn
Physikalisches Institut

Search for Same-sign Top Quark Pairs with Dimuon Final State in the ATLAS Experiment with 2 fb^{-1} of Data at $\sqrt{s} = 7$ TeV

Sara Ghasemi

The production of a pair of top quarks with same electric charges has been discussed as a signature for exotic colored states and also as a possible explanation for the observed deviation of top quark forward-backward asymmetry from the Standard model expectations at Tevatron. Therefore, a search for the same-sign top quark pair production is performed. As events with same-sign dimuon final states are very rare in the Standard model, the search is performed in this decay channel. The analysis uses the data from proton-proton collisions at 7 TeV center-of-mass energy at LHC, collected by ATLAS detector, with a total integrated luminosity of 2.05 fb^{-1}.

The analysis is based on cut and counting method. The background contribution is determined by using Monte Carlo simulations as well as data-driven methods. The observed number of events in data is consistent with the expected Standard model background within the uncertainties, therefore there is no evidence for new physics. The analysis result is used to set limits for various tt production models.

Physikalisches Institut der
Universität Bonn
Nußallee 12
D-53115 Bonn

BONN-IB-2012-13
July 2012

Universität Bonn
Physikalisches Institut

Search for Same-sign Top Quark Pairs with Dimuon Final State in the ATLAS Experiment with 2 fb^{-1} of Data at $\sqrt{s}$ = 7 TeV

Sara Ghasemi

Dieser Forschungsbericht wurde als Masterarbeit von der Mathematisch-Naturwissenschaftlichen Fakultät der Universität Bonn angenommen.

Angenommen am:	11.04.2012
Referent:	Prof. Dr. Norbert Wermes
Koreferentin:	Prof. Dr. Jochen Dingfelder

Acknowledgements

At this point I would like to offer my thanks and appreciation to all the people who shared their knowledge and experiences with me during the completion of this work.

I heartily thank my both supervisors Prof. Dr. Norbert Wermes and Dr. Markus Cristinziani from the physics institute of university of Bonn for all their help, guidance, patience and engagement from the initial to the final level of my thesis. I offer my thanks to all the group members of Top Quark Emmy Noether Group in university of Bonn, who helped me to develop a better understanding of the topic. I thank them for their contribution and their good-natured support. I also would like to thank Prof. Dr. Jochen Dingfelder who kindly accepted to be the co-referent of this thesis.

A heartfelt gratitude goes to Shahram Faridani for all the support and help I received from him.

Last but not least my deepest gratitude goes to my family, my parents Farideh Daraei and Ahmad Ghasemi as well as my sister Saba for their support and love not only during this work but throughout my whole life.

Contents

Chapter 1

Introduction

The Standard model of particle physics is an extremely successful theory and many of its predictions have been confirmed by precise measurements. However, some deficiencies of this model have been the motivation for new theories that extend the Standard model while encompassing it. On the other hand, the very successful operation of the large hadron collider at a new energy regime, opens a new chapter of searches for new physics models which have been hardly accessible before.

For exploring new physics, it is important to chose processes which their collider signature are novel, have relatively large cross section and their Standard model background are suppressed. Production of a pair of top quarks with same electric charge (same-sign top quark pair) satisfies these three key points.

The same-sign top quark pair production is a striking signature of the physics beyond the Standard model. Same-sign top quark pairs have been discussed as a signal for exotic colored states [10] [41]. Also, their production have been considered in possible explanations for the observed deviation of top quarks forward-backward asymmetry from the Standard model expectations at the Tevatron collider. In particular, models with the exchange of a real neutral boson in t-channel lead to same-sing top pair production [11]. Therefore, a search for same-sign top pairs places strong constraints on the models explaining the forward-backward asymmetry.

The same-sign top quark pairs are produced in interactions which are mediated by exotic boson fields. For the tt production from initial u-quarks, which is the subject process of this study, the possible new vector bosons are neutral color singlets or octets and charge $\frac{4}{3}$ color triplets or sextets and the possibilities for new scalar bosons are neutral color singlets or octets and charge $\frac{4}{3}$ color sextets [5].

The same-sign dimuon final state of same-sign top pair production has a very low background in the Standard model. Events with two high momentum leptons with same electric charges in the final state are very rare in the Standard model. Between electrons and muons, which are the leptons we can directly detect, muons are better reconstructed in the detector and their charge is better determined.

In this study, the model-independent production is considered. This is based on the assumption that the mediators are very heavy therefore the production interaction can be simplified to an effective four-fermion interaction. Moreover, the production by the exchange of a light neutral color-singlet boson in t-channel is studied too. It is done for three different boson masses which could be more directly related to the top quarks forward-backward asymmetry.

The analysis in this thesis is based on the cut and counting method. It means that by considering the expected experimental signature of the signal processes, certain cuts are designed and applied on the data samples to select the candidate signal events. The number of selected events are counted and used to interpret the search result.

Although the selection cuts are designed to reduce the number of background events, there are still background processes which contribute to the signal selection region. A careful evaluation of the background events is crucial for search analysis. The background contribution is determined by using Monte Carlo simulations and data-driven methods.

This analysis is performed on data samples collected by ATLAS detector in year 2011, from the proton-proton collisions at the large hadron collider, with the center-of-mass energy of 7 TeV. The data samples have an integrated luminosity of 2.05 fb^{-1}in total.

The result of the analysis is used to set limits on the same-sign top quark pair production models.

Chapter 2

Theory

This chapter gives a brief review of the *Standard Model* (SM) *of particle physics* [34] [7]. It only covers the most important aspects of the SM that are related to this study. Furthermore, the theoretical models of the same-sign top quark pair production are discussed in this chapter.

2.1 The Standard Model

The SM describes the fundamental particles and their interactions. This model has a structure of renormalizable field theory and is based on the local gauge symmetry of $SU(3)_C \times SU(2)_L \times U(1)_Y$. Three of the four fundamental interactions are included in the SM: the strong, the weak and the electromagnetic forces. The particle contents of the SM are the spin $\frac{1}{2}$ matter particles, known as *fermions*, and the spin 1 force carriers, known as *gauge bosons*. The interactions between matter particles are mediated by exchanging the corresponding gauge boson.

According to the SM, the basic constituents of the matter are twelve fermions classified to *quarks* and *leptons*. Each fermion has an antiparticle with the same mass and opposite electric charge. The names, symbols, masses and some quantum numbers of fermions are given in Figure 2.1. The quarks carry color charge and therefore interact via the strong interaction, whereas the leptons do not have color. While leptons exist as free particles, quarks can only exist in color-neutral bound states due to the *color confinement*. These bound states are known as *hadrons* and they contain either a quark and an antiquark (*mesons*) or three quarks (*baryons*). All fermions take part in the weak interaction since they all carry weak isospin. The fermions that have electric charge (i.e. all except neutrinos) interact via the electromagnetic interaction. In both classifications, fermions are grouped into pairs with identical properties except for mass, called *families* or *generations*. This is illustrated in Figure 2.1 too.

The gauge bosons consist of eight *gluons*, which mediate the strong interaction, Z, W^+ and W^- bosons, which mediate the weak interaction and the *photon* which is the mediator of the electromagnetic interaction (see Figure 2.1). Since the gluons carry color charge, in addition to mediating the strong interaction they can interact strongly among themselves. The strong interaction is described by the *Quantum Chromodynamics* (QCD) and its symmetry group is the $SU(3)_C$ factor of the SM gauge symmetry. This gauge group acts the same on left- and right-handed fermions [1]. The electromagnetic and weak forces are unified and described by *electroweak* theory with the $SU(2)_L \times U(1)_Y$ symmetry group. The $SU(2)$ part acts differently on the left- and right-handed fermions while the $U(1)$ gauge group does not discriminate the left- and right-handed fermions.

The only tree level interactions in the SM which change the fermion flavors are charged weak interactions. An up-type quark of a quark family turns into a down-type quark by emitting a W boson. The information on the strength of the flavor changing weak currents are contained in the 3×3 unitary *Cabibbo-Kobayashi-Maskawa* (CKM) *matrix*.

---

[1] The *helicity* measures the sign of the component of spin of the particle in the direction of motion [36] . The *right-handed* particles are the ones with helicity of +1 and the *left-handed* particles have helicity of -1.

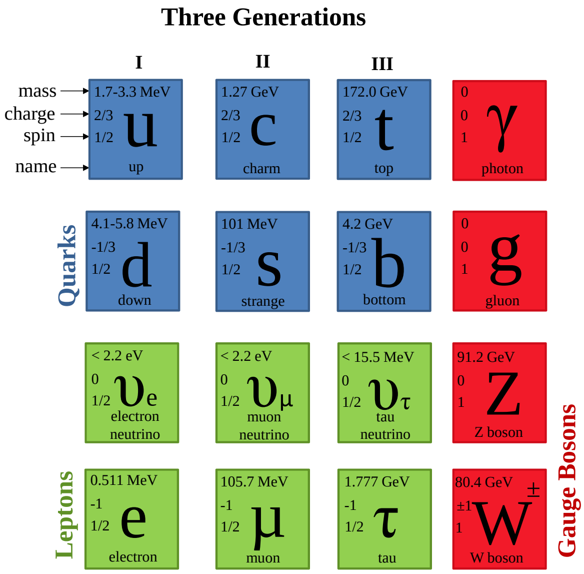

Figure 2.1: Particle content of the Standard Model that has been discovered so far. The masses are taken from [32].

The gluons and the photon are massless as a consequence of the exact conservation of the corresponding symmetry generators, the electric charge and the color charges. The weak gauge bosons, Z and $W^{\pm}$, however, have large masses, indicating that $SU(2)_L \times U(1)_Y$ is not a symmetry of the vacuum. In the SM, the spontaneous breaking of the electroweak gauge symmetry is implemented by the so called *Higgs mechanism*. This provides the proper masses for the weak bosons and also the fermions. The consequence of the Higgs mechanism is the prediction of the presence of a new massive neutral particle, Higgs boson, associated to a scalar (spin 0) field. The Higgs boson has not been observed yet and is the last remaining piece that would complete the theory of SM.

2.2 Same-sign Top Quark Pairs

In the SM, top quarks are produced at hadron colliders through two main mechanism: predominantly, as top-antitop ($t\bar{t}$) pairs via the strong interaction, and in a lower rate, as single top quarks via the weak interaction.

Production of a pair of top quarks with the same electric charges (tt or $\bar{t}\bar{t}$) is absent in the SM at the tree level. The same-sign top pair production is described by new physics models that expand the SM while encompassing it. These extensions satisfy the $SU(3)_C \times SU(2)_L \times U(1)_Y$ gauge invariance of the SM.

At hadron colliders, same-sign top pairs can only be produced from initial up or charm quarks due to the charge conservation. As the LHC is a proton-proton collider, the scattering process with two u-quarks in the initial state is enhanced by the large parton[2] luminosity of the valance quarks. So the sensitivity of $uu \rightarrow tt$ at the LHC is far better than the processes with one or two initial c-quarks, therefore this research is concentrate on this process.

---

[2] Proton constituents. At high energy scales they are two valence u-quarks, one valance d-quark, sea quarks and antiquarks and gluons.

The $uu \to tt$ process is mediated by new boson fields. Since the new interactions must fulfill the SM gauge symmetry, new fields have restricted quantum numbers. Assuming renormalizable interactions, they can be either vector bosons (spin 1) or scalars (spin 0). The possibilities for the new vector bosons mediating this interaction at tree level are [5] :

- a neutral boson, Z', which is a singlet $SU(3)_C$ representation (color-singlet) and can be either in a singlet $SU(2)_L$ representation (isosinglet, denoted by $\mathcal{B}_\mu$) or belong to a triplet $SU(2)_L$ representation (isotriplet, denoted by $\mathcal{W}_\mu$)
- a neutral color-octet, g', which is either an isosinglet ($\mathcal{G}_\mu$) or a member to an isotriplet ($\mathcal{H}_\mu$)
- a charge $\frac{4}{3}$ color-triplet particle which is a component of an isodoublet ($\mathcal{Q}^5_\mu$)
- a charge $\frac{4}{3}$ color-sextet particle which belongs to an isodoublet ($\mathcal{Y}^5_\mu$)

and the possible scalars are [5] :

- a neutral member of an isodoublet, which can be a color singlet (ϕ) or color octet (Φ)
- a charge $\frac{4}{3}$ color-sextet, which can be either an isosinglet (Ω^4) or a component of an isotriplet (Σ)

The particles with charge $\frac{4}{3}$ are exchanged in s-channel and the neutral ones are exchanged in t-channel. Figures 2.2 (a) and (b) show the corresponding Feynman diagrams.

The model-independent parametrization of a process is the most convenient and economical way to search for new physics. If the new bosons are heavy enough, i.e. have masses above the electroweak symmetry breaking scale v and, for consistency, larger than the partonic center-of-mass energy, their contribution to $uu \to tt$ process can be described by an effective low-energy Lagrangian. In this case, the new bosons lie at a higher energy scale and their effect at lower energies is parametrized by an effective Lagrangian which involves only the SM fields.

Therefore all the six possible models with vector bosons and four possibilities for scalers can be described by a gauge-invariant effective four-fermion interaction, as shown in Figure 2.2 (c), for heavy mediators. The effective Lagrangian is of the general form of [4] :

$$\mathcal{L}^{eff} = \sum \frac{C_x}{\Lambda^2} O_x + ... \tag{2.1}$$

where O_x are dimension-six gauge-invariant operators, C_x are complex constants and Λ is the new physics scale. Effects of dimension-eight and higher-order operators are suppressed by at least $1/\Lambda^4$ and are ignored. The complete set of dimension-six operators involving two same-sign top quarks is introduced in [20] .

Those operators generate the relevant terms of the effective four-fermion Lagrangian for the $uu \to tt$ process [6] :

$$\begin{aligned}\mathcal{L}^{uu\to tt}_{4F} = & \frac{1}{2}\frac{C_{LL}}{\Lambda^2}(\bar{u}_L\gamma^\mu t_L)(\bar{u}_L\gamma_\mu t_L) + \frac{1}{2}\frac{C_{RR}}{\Lambda^2}(\bar{u}_R\gamma^\mu t_R)(\bar{u}_R\gamma_\mu t_R) \\ & - \frac{1}{2}\frac{C_{LR}}{\Lambda^2}(\bar{u}_L\gamma^\mu t_L)(\bar{u}_R\gamma_\mu t_R) - \frac{1}{2}\frac{C'_{LR}}{\Lambda^2}(\bar{u}_{La}\gamma^\mu t_{Lb})(\bar{u}_{Rb}\gamma_\mu t_{Ra}) \\ & + \text{h.c.}\end{aligned} \tag{2.2}$$

where the sub-indices L and R denote the left- and right-handed fermions, a and b in the last term indicates the color contractions and γ^μ are the gamma matrices. Only four independent terms appear in the Lagrangian since there are two pairs of identical particles involved except for the color indices.

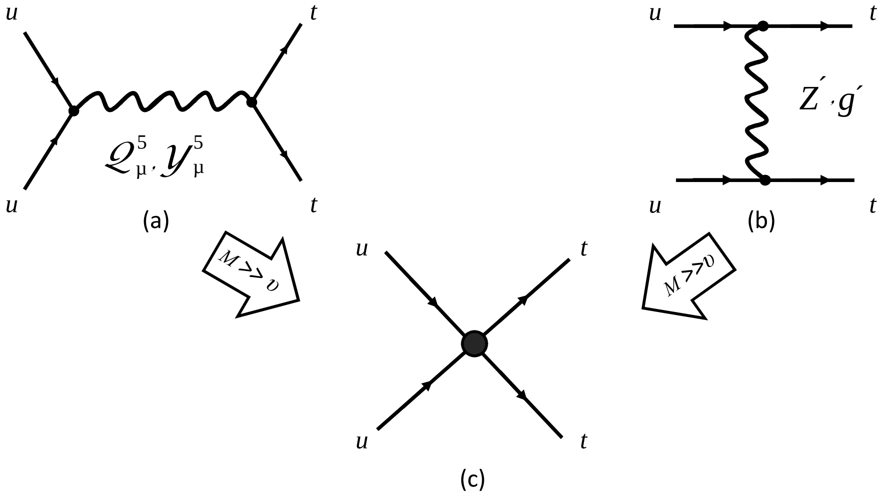

Figure 2.2: Production of same-sign top quark pairs from initial u-quarks via exchange of a vector boson in s-channel (a) or in t-channel (b). For large boson masses, all the cases can be described by an effective four-fermion interaction (c).

The cross section for the process $uu \rightarrow tt$ at the LHC for the center-of-mass energy of 7 TeV is evaluated to be [6] :

$$\begin{aligned}\sigma(tt) = &\frac{16.0}{\Lambda^4}[|C_{LL}|^2 + |C_{RR}|^2] \\ &+ \frac{2.00}{\Lambda^4}[|C_{LR}|^2 + |C'_{LR}|^2] + \frac{0.96}{\Lambda^4} Re\, C_{LR}C'_{LR}\end{aligned} \tag{2.3}$$

where the numerical values in the coefficients are calculated in pb × TeV^4.

For the fixed value of $|C|/\Lambda^2 = 1\text{TeV}^{-2}$, the inclusive cross section of $uu \rightarrow tt$ for same-sign top quarks with identical helicity states ($t_R t_R$ and $t_L t_L$) is 8 pb and for the same-sign top quarks with opposite helicity states ($t_L t_R$) is 2.4 pb. The cross section for $\bar{u}\bar{u} \rightarrow \bar{t}\bar{t}$ is around 100 times smaller. The cross section of same-sign (anti-)top quarks production [3] is more than three orders of magnitude smaller than the above numbers [6] .

Among all the models of same-sign top pair production, the interaction with exchange of a flavor-violating Z' boson in the t-channel is particularly interesting. It has been discussed as a possible explanation for the anomalously large $t\bar{t}$ forward-backward asymmetry (A_{FB}) observed at Tevatron [11] . The definition of A_{FB} is given in Appendix A. The Z' model produces top quarks in the forward region and its contribution to the SM production of $t\bar{t}$ can enhance the A_{FB}. Therefore a search for same-sign top

---

[3] As Tevatron is a proton-antiproton collider, the cross sections of $uu \rightarrow tt$ and $\bar{u}\bar{u} \rightarrow \bar{t}\bar{t}$ are equal.

quark pairs puts a strong restriction on models explaining the $t\bar{t}$ forward-backward asymmetry.

The Lagrangian which contains the flavor changing neutral current of u-t-Z' has a form of [11] :

$$\mathcal{L} = g_W \, \bar{u} \, \gamma^\mu \, (f_L P_L + f_R P_R) \, t \, Z'_\mu + \text{h.c.} \tag{2.4}$$

where g_W denotes the weak coupling strength and $f_{L(R)}$ is the left-(right-)handed coupling. The left-handed coupling is highly constrained by B_d-$\bar{B}_d$ mixing [11], therefore only the production of right-handed top quarks are considered.

Since the models with the exchange of a heavy Z' boson in the t-channel are ruled out as the sole explanation of the observed deviation of $\mathrm{A_{FB}}$ [5] , in this research the light Z' bosons with masses of 100, 150 and 200 GeV are studied. The corresponding cross sections, which are filtered and weighted for the desired final state, can be seen in Table 4.1.

Chapter 3

Experimental Environment

3.1 The Large Hadron Collider

The *Large Hadron Collider* (LHC) [12] [13] is a circular particle collider at CERN (the European Organization for Nuclear Research), designed to collide proton-proton (p-p) or lead ion pairs. The LHC is installed in the tunnel which was formerly used for the *Large Electron Positron collider* (LEP); a tunnel with 27 kilometer circumference at about 100 meters (in average) underground, beneath the France-Switzerland border, near Geneva (see Figure 3.1).

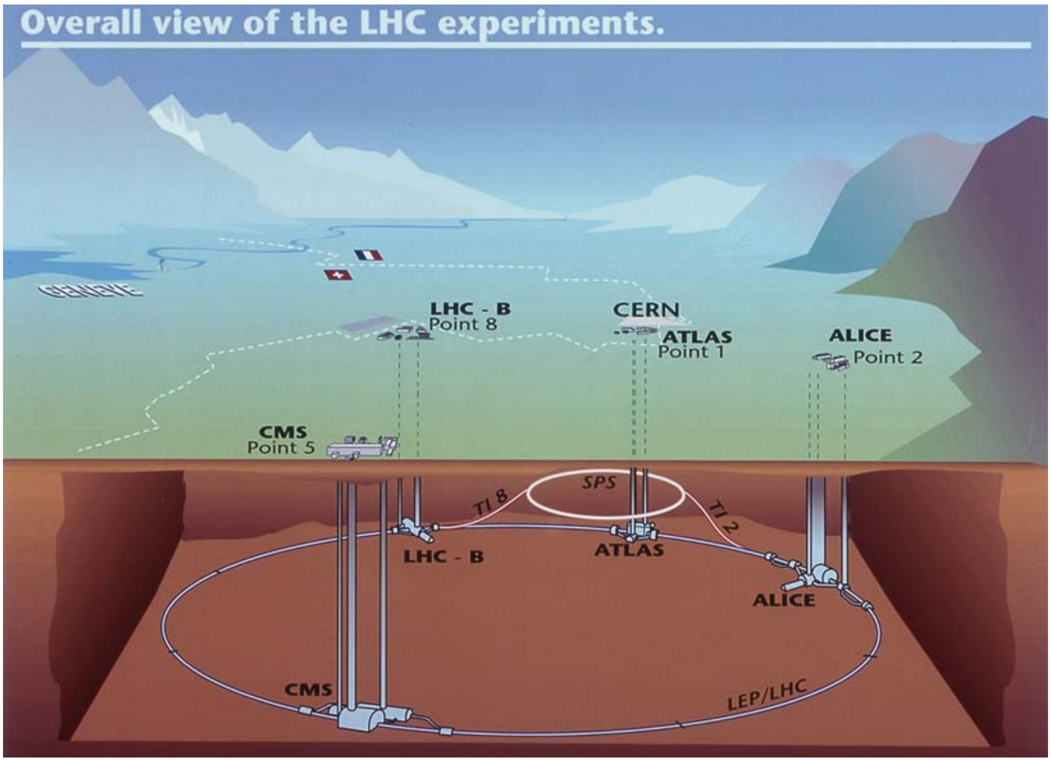

Figure 3.1: The location of LHC and its four main experiments. (ATLAS Experiment ©2012 CERN)

For proton-proton collisions, the LHC is designed to accelerate the two proton beams circulating in opposite directions to reach the beam energy of 7 TeV, leading to a center-of-mass energy ($\sqrt{s}$) of 14 TeV for the collision. The designed peak instant luminosity of LHC is 10^{34} cm^{-2}s^{-1}. The protons are bunched together in the beam and at the peak luminosity there are 2808 bunches per beam, each carrying 1.15×10^{11} protons, with 25 ns time interval between the bunches, leading to a collision frequency of 40 MHz.

The protons are accelerated in several steps to reach the final beam energy. Before entering the LHC main ring, they are accelerated up to 450 GeV in already existing accelerator facilities which form the injector chain. When they are circulating in the LHC main ring to reach their final energy, 1232 superconducting dipole magnets with maximum field of 8.33 T keep them in their circular path, while 392 quadrupole magnets focus the beams. The magnets are cooled by super-fluid helium to the operating temperature of 1.9 K.

The beams are brought to collide in four points along the main ring where the ATLAS, the CMS, the ALICE and the LHC-b detectors are positioned (see Figure 3.1). The two large detectors, ATLAS and CMS, are the multi-purpose detectors, designed to cover the largest range of physics possible. The reason of having two independently designed detectors with the same application is to cross-confirmation of any new discoveries made. ALICE and LHC-b are two medium size experiments with specialized detectors. LHC-b is specialized to study the *b*-quarks in order to investigate the matter-antimatter differences while ALICE is the dedicated detector for heavy ion collisions.

The first recorded proton–proton collisions provided by the LHC had a center-of-mass energy of 900 GeV and were recorded in November 2009 [39] . From March 30th 2010 [37] the LHC is running with the beam energy of 3.5 TeV, providing a center-of-mass energy of 7 TeV. The LHC will operate at 4 TeV per beam in 2012. It is scheduled to run until November 2012, then there will be a long technical shutdown with the LHC restarting close to its full design energy late in 2014 [38] .

3.2 The ATLAS Detector

ATLAS (***A* *T**oroidal* ***LHC* *A**pparatus*) [1] [2] is a multi-purpose particle detector constructed around one of the four interaction points of the LHC. This detector with 44 m long, 25 m diameter and about 7000 tons weight covers almost the full solid angle. The detector is composed out of a barrel part which surrounds the beam pipe cylindrically and the two endcaps which are perpendicular to the beam axis.

ATLAS uses a right-handed coordinate system with its origin at the nominal interaction point in the center of the detector. The z-axis is along the beam pipe, the x-axis points to the center of the LHC ring and the y-axis points upward. The cylindrical coordinates (r,ϕ) are used in the transverse plane (x-y plane) with ϕ being the azimuthal angle around the beam pipe. The polar angle, θ, is measured with respect to the beam axis, but more commonly the *pseudorapidity* is used which is defined as:

$$\eta = -\ln\tan\frac{\theta}{2} \tag{3.1}$$

and in terms of the momentum, it can be written as:

$$\eta = \frac{1}{2}\ln(\frac{p + p_z}{p - p_z}) \tag{3.2}$$

The distance in η-ϕ space is usually measured by:

$$\Delta R = \sqrt{\Delta\phi^2 + \Delta\eta^2} \tag{3.3}$$

The ATLAS detector is composed of three main sub-detectors: the inner detector (ID), the calorimeter and the muon spectrometer (MS).

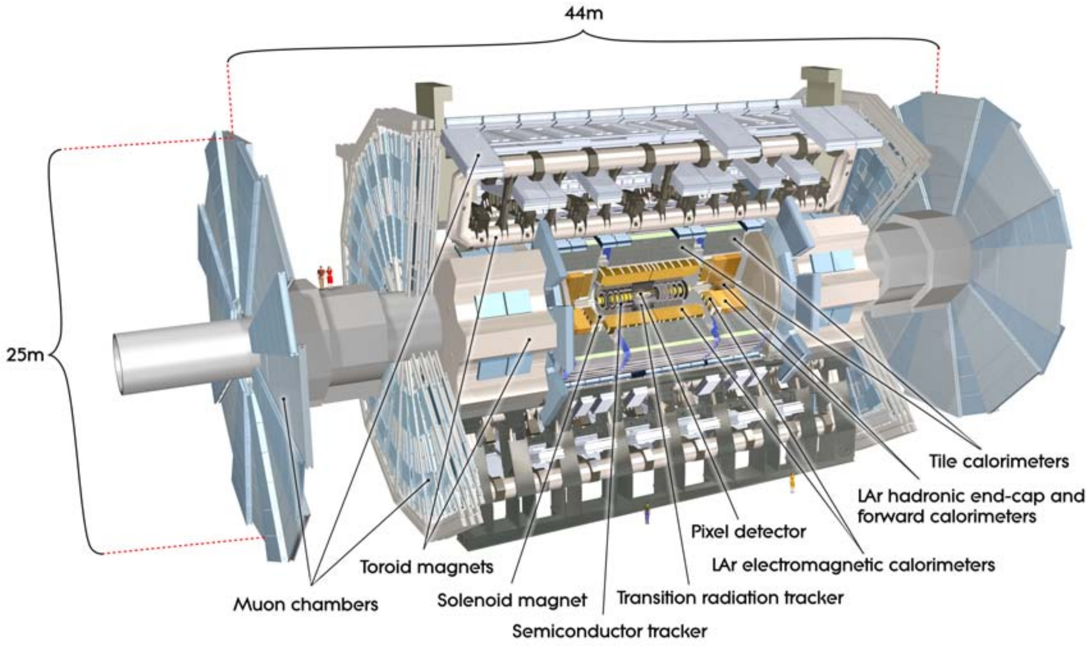

Figure 3.2: Cut-away view of the ATLAS detector (ATLAS Experiment ©2012 CERN).

3.2.1 Inner Detector

The ID [3] is the closest ATLAS sub-detector to the beam pipe. It has a cylindrical shape with 1.15 m radius and 5.5 m length and surrounds the beam pipe which has a radius of 36 mm. It is immersed in a 2 T solenoid field and provides the information for reconstructing the tracks of charged particles and measuring their momenta and charges. The vertex reconstruction is achieved by ID measurements.

The ID consists of three different sub-detectors which can be seen in Figure 3.3: the *pixel detector*, the *semiconductor tracker* (SCT) and the *transition radiation tracker* (TRT).

The pixel detector is the most inner sub-detector of ATLAS. Its fine granularity provides the high resolution needed close to the interaction point in order to resolve the tracks from a primary collision or a secondary vertex. With its special structure, a very good transverse impact parameter measurement and a three dimensional vertexing is possible.

The pixel detector is a silicon detector, built from 1744 pixel modules. The nominal size of a pixel is $50 \times 400 \mu\text{m}^2$. The modules are arranged in three cylindrical barrel layers and two endcaps on the sides of barrel, with three discs in each of them. With this structure, three hits for each track are possible and it can cover a range of $|\eta| < 2.5$. The most inner layer of the pixel detector is called b-layer, as it is very important for identification and reconstruction of secondary vertices in decay of the hadrons containing b-quarks. Each module has 46080 active readout cells, leading to a total 80.4 million readout channels for pixel detector which are about 50 % of all the readout channels of ATLAS detector [3].

The SCT is located around the pixel detector with four cylindrical barrel layers and two end-caps on barrel sides with nine discs on each of them. Its functionality is similar to the pixel detector, but its larger surfaces allows to measure tracks in a longer distance. Since there is lower occupancy in this part, using micro-strip instead of pixels is good enough to have the required accuracy of measurements. The SCT layers have silicon micro-strip detectors with 768 readout strips, each with 80 μm pitch. The total

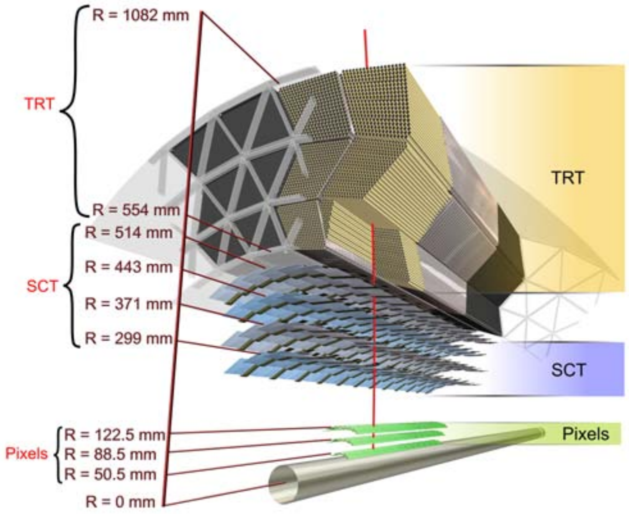

Figure 3.3: Scheme of the ATLAS inner detector barrel being crossed by one high-energy particle. (ATLAS Experiment ©2012 CERN)

number of readout channels in SCT is 6.2 millions [3].

The outer part of the ID is the TRT which is made from straw tubes. The straws are parallel to the beam axis in the barrel and they are arranged radially in the end-caps. Each straw tube has 4 mm diameter. The TRT records a large number of hits, typically 30, for each track within $|\eta| < 2.0$. It provides the information for electron identification by absorbing and measuring the photons from the transition radiations. The characteristic radiation is used to separate electrons from hadrons like pions. The total number of readout channels in TRT is about 351000 [3].

3.2.2 Calorimeter

The calorimeter measures the energy of charged and neutral particles. It covers a range of $|\eta| < 4.9$ which is very critical for a precise measurement of the missing transverse momentum (see Section 4.4.3). The particles must deposit their entire energy to the bulk of matter in the calorimeter. Therefore, the calorimeter must provide a good containment for them.

The calorimeter has two subsystems: the electromagnetic (EM) calorimeter and the hadron calorimeter. Photons and electrons deposit their energy in EM calorimeter and for hadrons it happens in hadron calorimeter. Muons pass all the way through the calorimeter system and enter the muon spectrometer. The layout of ATLAS calorimeter can be seen in Figure 3.4.

The EM calorimeter is divided into a barrel part and two end-caps (EMEC) , each housed in their own cryostat. The barrel calorimeter covers the range of $|\eta| <$ and consists of two identical half-barrels which are separated by a small gap (4 mm) at $z = 0$. Each endcap components is divided to two coaxial wheels, the outer one covers $1.375 < |\eta| < 2.5$ and the inner one covers $2.5 < |\eta| < 3.2$.

The EM calorimeter is a lead-Liquid Argon (LAr) calorimeter with accordion-shaped geometry. The electrons and photons loose their energy by undergoing bremsstrahlung and pair production, leading to form electromagnetic showers. The liquid Argon is the active medium and lead plates are the absorber.

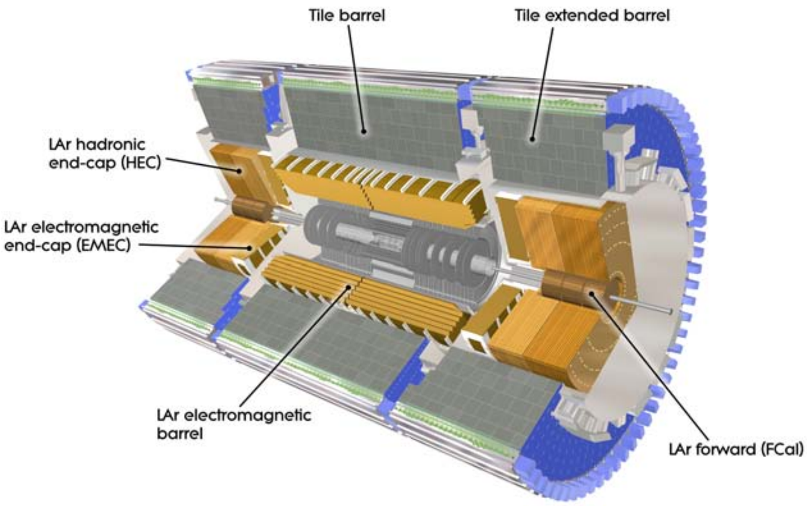

Figure 3.4: Cut-away view of the full calorimeter system of ATLAS. (ATLAS Experiment ©2012 CERN)

The total thickness of EM calorimeter in the barrel is larger than 22 radiation lengths[1] and in the endcaps larger then 24 radiation lengths [17] .

The hadron calorimeter needs to have a larger size than the EM calorimeter since the average nuclear interaction length is larger than the average radiation length. The hadron calorimeter itself has tree different components: the tile barrel, the hadron endcap calorimeter (HEC) and the forward calorimeter (FCal).

The tile calorimeter is located directly behind the EM calorimeter and composed out of a central barrel which covers $|\eta| < 1.0$ and two extended barrels with a coverage range of $0.8 < |\eta| < 1.7$. The scintillating tiles are the active material and steel plays the role of absorber. Its total thickness at the outer edge of the tile-instrumented region is 9.7 interaction length at $|\eta| = 0$ [17].

HEC and FCal both are LAr calorimeters. The LEC components are placed directly behind the endcaps of EM calorimeter and share the same LAr cryostat. Each endcap consists of two independent wheels and covers the range of $1.5 < |\eta| < 3.2$. The FCal components cover $3.1 < |\eta| < 4.9$ in order to provide a large solid angle coverage which would be very important for missing transverse energy measurement [17].

3.2.3 Muon Spectrometer

The MS is the largest and outermost part of the ATLAS detector. As mentioned before, muons fly through the calorimeter and do not deposit so much energy there. Therefore another system, the MS, is needed to detect the muons which penetrate other elements of the detector. MS provides information for reconstructing the muon tracks and measuring their momenta and charges, based on the concept of magnetic deflection of muon tracks in the large superconducting toroid magnets. The MS layout is shown in Figure 3.5 together with the toroid magnet system.

The toroid magnets is made of a barrel and two endcaps. Over the range of $|\eta| < 1.4$, muon tracks are bent by the barrel toroid and in the $1.6 < |\eta| < 2.7$ region, magnetic bending is provided by endcap fields.

---

[1] The radiation length is the length at which the particle holds $1/e$ fraction of its initial energy.

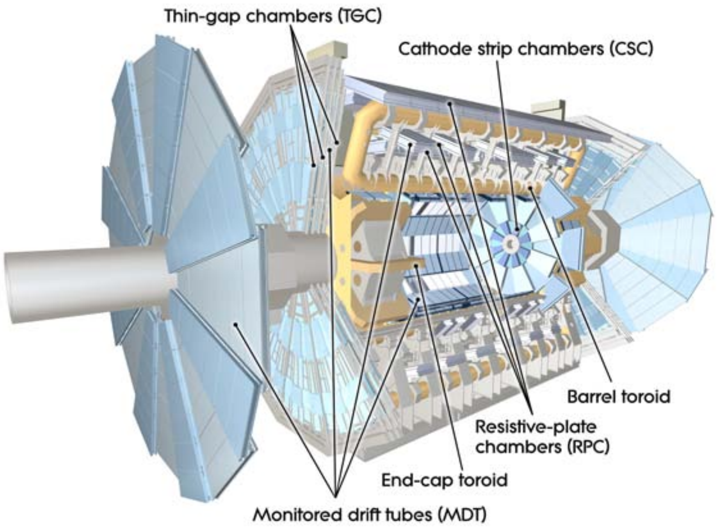

Figure 3.5: Cut-away view of the ATLAS muon system. (ATLAS Experiment ©2012 CERN)

In the region of $1.4 < |\eta| < 1.6$ which is usually referred as the transition region, magnetic deflection is due to the combination of barrel and endcap fields.

The MS is composed out of two main subsystems, the precision chambers that measure the track positions, and the trigger chambers that identify muon tracks within the time to the next bunch crossing. The precision chambers consist of Monitored Drift Tubes (MDT's) and Cathode-Strip Chambers (CSC's), and the trigger chambers consist of Resistive Plate Chambers (RPC's) and Thin Gap Chambers (TGC's).

The MDT's have three to eight layers of drift tubes and provide a precision measurement of the track coordinates over $|\eta| < 2.7$. The CSC's are used in the forward region over $2 < |\eta| < 2.7$ as they have higher granularity. They are multi-wire proportional chambers with cathodes segmented into strips. The trigger system covers the range of $|\eta| < 2.4$ by using RPC's in the barrel region and TGC's in the endcap region. The trigger chambers provide bunch-crossing identification and well-defined transverse momentum thresholds and they measure the muon coordinate in the direction orthogonal to that determined by the precision-tracking chambers [17].

3.2.4 Trigger System

The collisions at LHC happen in such a high rate that it is not possible to record all the data due to the limited rate of writing data to storage. On the other hand, not all of the interaction processes are of interest. There are many minimum bias events which are not the target of analysis for the physics we want to study. Therefore a trigger system is needed to select and storage the interesting processes for future offline analysis.

The ATLAS trigger system selects the events in three levels: Level-1 (L1), Level-2 (L2), and Event Filter (EF).

The L1 trigger searches for high transverse momentum muons, electrons/photons, jets, and τ leptons decaying to hadrons and also selects the events with high missing transverse energy large total transition energy. It uses the information of RPC and TGC subsystems of muon spectrometer for muons and calorimeter systems for all other objects. The L1 trigger system reduces the number of events from the starting rate of 40 MHz to a rate less than 75 kHz.

The L2 trigger on the other hand is a software based trigger system and seeded by Regions-of-Interest (RoI). These are the regions of detector where the L1 trigger has already identified interesting objects within them. The L2 trigger uses RoI information on coordinates, energy, and type of signatures to reduces the event rate to below 3.5 kHz.

The last trigger level is EF which uses offline analysis procedures on fully-built events to further event selecting. It reduces the event rate down to approximately 200 Hz which is a rate in which the events can be recorded for subsequent offline analysis [17].

Chapter 4

Analysis Strategy

In this chapter, after defining some important variables, the signal process with its experimental signature is introduced. The background processes which are the events that mimic the same signature are introduced as well. In the following section of the chapter, the data and Monte Carlo samples which are used for the analysis are described. The object and event selection cuts, which are applied to select the candidate signal event from the data samples, are presented in the last section of the chapter.

4.1 Important Variables

It would be useful to give the definition of some important variables at this point, since they are going to be used very frequently in this chapter and the rest of this thesis.

The center-of-mass energy of proton-proton collisions at the LHC is well defined. The energies of the two proton beams are known and by summing them up we get the center-of-mass energy of collision. But when a collision happens, the (anti)quarks and gluons which are the proton constituents interact, rather than the protons themselves. The proton constituents, or partons, carry a fraction of proton momentum which is undefined for us. Therefore, the center-of-mass energy of the interaction is unknown. Also, when partons with different momentum fractions collide, the interaction system is boosted by an unknown size in the z direction. The only well define kinematic variable of the interaction therefore, is the transverse momentum:

$$\vec{p_T} = (p_x, p_y)$$

Since the colliding partons do not have momentum in the transverse direction, the sum of the transverse component of momentum of all outgoing particles is expected to be zero. Any deviation from zero could indicate the presence of particles which are not detected. This fact is used to recover the information about the invisible particles, such as neutrinos, by defining the *missing transverse energy*:

$$\vec{E_T^{\text{miss}}} = -\sum \vec{E_T}$$

$\vec{E_T}$ is the vectorial sum of the calorimeter cell entries in the transverse plane.

In the analysis usually the absolute values of the $\vec{p_T}$ and $\vec{E_T^{\text{miss}}}$ vectors are used.

The variables which describe the event topology are already introduced in Section 3.2, when the ATLAS coordinate system is presented.

4.2 Signal and Background Processes

Top quarks decay almost exclusively to a bottom quark and a W boson through weak interaction. The decay of top quarks to strange or down quarks are strongly suppressed by the CKM matrix[1]. The W boson can decay hadronically, into two quarks, or leptonically, into a lepton and a neutrino.

In this study, only the dimuon final state is considered, when both W bosons originated from the top pair, decay to muons. As the top quarks have same electric charges, the muons in the final state are same-sign as well.

The b-quarks in the final state hadronize in the detector and form jets. Additional jets in the event are possible, due to the QCD emissions. the additional jets are expected to have low p_T.

The two neutrinos in the final state escape the detector without being detected, as they are neutral and interact with matter very weakly. They are reconstructed as E_T^{miss} in the detector.

In summary, the expected experimental signature of the signal process is: two same-sign high-p_T and isolated muons, at least two jets and high E_T^{miss}.

There are several events that mimic the same signature in the detector. It is mostly because of the mis-reconstructed muons. These are muons which are usually originated from a b- or c-hadron decay. Also the wrong measurement of muon charge could lead to background events. It happens when in a process with opposite-sign muons, the charge of one of the muons is mis-identified. Apart from these two sources which are completely detector dependent, there are several SM process with real same-sign dimuons in the final state. These processes are very rare, but usually they are irreducible. The background processes are described in more detail in Chapter 5.

4.3 Data and Monte Carlo Samples Description

4.3.1 Data

The data used in this study were collected by the ATLAS detector in 2011, when the LHC was running with 7 TeV center-of-mass energy.

The data taking is separated into periods. Each period represents data with a coherent configuration of the detector and the trigger system [25] . The data-taking periods that are used are labeled from B2 to K.

The luminosity is measured and stored for small time intervals called *luminosity blocks* for which the integrated luminosity can be determined [8]. The total integrated luminosity over time is integrated over the luminosity blocks. For the data sample used in this study, the total integrated luminosity is 2052.49 pb^{-1}.

The data samples are reconstructed with the ATLAS software of release 16.

4.3.2 Monte Carlo

The Mont Carlo (MC) simulation is used to calculate the acceptance for the signal events and to determine the contribution from background processes. The MC samples are provided by MC10b production campaign of the ATLAS Production Group [26] .

---

[1] This is of course only based on the SM and without considering the flavor changing currents through the exchange of new bosons that are introduced in Section 2.2.

Signal Samples

The signal processes are described in Section 2.2. Two sets of signal samples are used:

- The samples which simulate the tt production from initial uu state by exchanging heavy mediators. The interaction is approximated by an effective four-fermion interaction.
- The simulation of tt production from light Z' boson exchange in t-channel for the masses of $m_{Z'}$ = 100, 150 and 200 GeV.

The dileptonic decay of tt are generated with PROTOS and showered with PYTHIA in both sets of signal samples. The samples are listed in Table 4.1. The cross sections are corresponded to a fixed value of $|C|/\Lambda^2 = 1$ TeV^{-2} (see Section 2.2). For the Z' models, $\Lambda = m_{Z'}$ in each case in the fix value of $|C|/\Lambda^2 = 1$ TeV^{-2} [6].

Sample number	Sample	σ[pb] × BR/Filter efficiency
119264	t_Lt_L from heavy mediators, dileptonic channel	1.77
119265	t_Lt_R from heavy mediators, dileptonic channel	0.22
119266	t_Rt_R from heavy mediators, dileptonic channel	1.77
119891	t_Rt_R from Z' with $m = 100$ GeV, dileptonic channel	0.0176
119892	t_Rt_R from Z' with $m = 150$ GeV, dileptonic channel	0.0366
119893	t_Rt_R from Z' with $m = 200$ GeV, dileptonic channel	0.0623

Table 4.1: Signal Monte Carlo samples and the cross sections of the corresponding processes. The cross sections are taken from [6].

Background Samples

Background processes are introduced in Section 4.2 and described with detail in Chapter 5. The MC samples of the following background processes are used:

- top-antitop pair production, generated for the nominal value of top mass (172.5 GeV)
- single-top production, generated for the nominal value of top mass (172.5 GeV)
- Z boson production
- diboson productions (W^+W^-, WZ, ZZ and $W^\pm W^\pm$ + 2jets)
- $t\bar{t}W$, $t\bar{t}W$ +jet, $t\bar{t}Z$, $t\bar{t}Z$ +jet, $t\bar{t}W^+W^-$

The background MC samples, their generators and the cross section of the corresponding processes are listed in the tables of Appendix B.

Pile-up Correction

When two crossing bunches in the beam collide, due to the large number of particles per bunch more than one collision can occur simultaneously. The presence of more than one interaction in the same bunch crossing is called pile-up. This effect has to be included in the analysis.

The MC simulations include the simulation of the underlying minimum bias events in addition to the main simulated process. In the simulation, the number of additional events for each simulated event is chosen from a Poisson distribution with the average number of $\langle\mu\rangle$.

In data, on the other hand, the average number of interactions in a collision is estimated for each luminosity block by $\langle\mu\rangle = \frac{L_{\text{inst}} \times \sigma_{\text{total}}}{N_{\text{bunches}} \times fr}$ where L_{inst} is the instant luminosity measured in the luminosity block, σ_{total} is the total inelastic cross section, N_{bunches} is the number of colliding bunches and fr is the revolution frequency.

The MC samples are weighted such that $\langle\mu\rangle$ distribution of MC matches the $\langle\mu\rangle$ distribution of data, in order to describe the pile-up effect correctly [16].

4.4 Object and Event Selection

4.4.1 Muons

The muons used in this study are combined muons, reconstructed by one of the ATLAS muon reconstruction chain algorithms called Muid [24] . It means that the information from both MS and ID subsystems are used to reconstruct the muon object.

The reconstruction in the MS starts by fitting the close hits in the same chamber station in a straight line to produce segments. Segments from the three chamber stations are fitted into a whole MS track. Then the MS track is extrapolated back to the interaction point through the calorimeter. The extrapolated MS track and ID track which are two independently measured tracks, are matched and combined to form a single track. This combination is done by performing a global refit by using all original hits in both ID and MS.

The muons are required to pass the track quality criteria recommended by ATLAS Muon Combined Performance [23]. The inner detector track must fulfill the following hit requirements:

- Number of B-Layer hits > 0 if the muon traverses an active pixel B-layer module
- Number of pixel hits + number of crossed dead pixel sensors > 1
- Number of SCT hits + number of crossed dead SCT sensors > 5
- Number of pixel holes + number of SCT holes < 2
- A successful TRT extension in the η acceptance of the TRT. It means, with n = number of TRT hits + number of TRT outliers:
    - for $|\eta| < 1.9$ require $n > 5$ and number of TRT outliers $< 0.9\ n$
    - for $|\eta| \geqslant 1.9$ if $n > 5$ then require number of TRT outliers $< 0.9\ n$

The isolation cuts are used to reject the background muons coming from decays of c- and b-hadrons. The calorimeter based isolation cut requires that the reconstructed energy in a cone of $\Delta R = 0.3$ around the muon candidate direction, after subtracting the muon energy itself, must be less than 4 GeV ($E_T^{cone\Delta R=0.3} <$ 4GeV). The tracking based isolation cut is similar, except that instead of the energy the scalar sum of p_T of tracks in the cone is used ($p_T^{cone\Delta R=0.3} <$ 4GeV). In addition, muons within a distance of $\Delta R < 0.4$ from any reconstructed jet with $p_T > 20$ GeV are removed.

To reject muons arising from cosmic rays, the events containing a muon pair that are back-to-back in the transverse plane and have transverse impact parameter relative to the beam axis of the value $|d_0| >$ 0.5 mm are removed.

The muons are required to have the transverse momentum of $p_T > 20$ GeV and to be from the central region of detector, $|\eta|$<2.5.

Finally, In order to reduce the background due to the muon charge mis-identification, It is required that the charge of the muon track measured in the inner detector and the charge of the extrapolated muon system track to be the same: $Q_{ID} = Q_{MS}$.

The muon selection cuts are identical with the common object selection of the Top Group of ATLAS [30], except for the $Q_{ID} = Q_{MS}$ cut.

4.4.2 Jets

Jets are reconstructed by the anti-k_t jet reconstruction algorithm of ATLAS. The jets with negative energy are removed. Only the jets with $p_T > 25$ GeV and $|\eta|$<2.5 are considered.

Jet quality criteria are applied to removed the so called bad jets which are the jets not associated to real energy deposits in the calorimeters [22] .

Electrons can be independently reconstructed as jets because of their shower shape in the electromagnetic calorimeter. It leads to the double-counting of objects. To avoid this, the jets overlapping with accepted electrons within $\Delta R < 0.2$ distance are removed [27] .

The b-jets are discriminated from light quark jets mainly due to the relatively long life time of b-hadrons. This results to a significant flight path before decaying and forms a secondary vertex which is measurable in the detector. This can be used for Identification of jets originating from b-quarks which is called b-tagging. The b-tagging algorithm used in this study is JetFitterCombNN with 80%efficiency [21] .

4.4.3 Missing Transverse Energy

For E_T^{miss} reconstruction, an object-based algorithm is used. It starts from the reconstructed objects in the event and uses their calorimeter clusters. Muons, which are not measured by the calorimeter, are included using their momentum measured from the ID and MS tracks. The topological calorimeter clusters, associated to electrons, high p_T jets and low p_T jets (*soft jets*), are used after calibration at the electromagnetic scale and correction according to the energy scale of the object. Then E_T^{miss} is calculated from [14] :

$$E_{x,y}^{\text{miss}} = E_{x,y}^{\text{electrons}} + E_{x,y}^{\text{jets}} + E_{x,y}^{\text{soft jets}} + E_{x,y}^{\text{muons}} + E_{x,y}^{\text{CellOut}} \tag{4.1}$$

$$E_T^{\text{miss}} = \sqrt{(E_x^{\text{mis}})^2 + (E_y^{\text{mis}})^2} \tag{4.2}$$

The CellOut term includes the remaining clusters not associated with the high p_T objects.

4.4.4 Event Selection

The event selection criteria used to select the signal events and reduce the background are listed below. The cut flows and cut efficiencies are summarized for background and two of signal samples in Table 4.2.

- **Trigger**: For data, the dimuon events are required to be selected online by a single muon trigger of:
    - EF-mu18 for data periods from B2 to I
    - EF-mu18-medium for data periods J and K

The p_T threshold of these event filters (see Section 3.2.4) are 18 GeV.

MC events have to be treated differently. The muon trigger in MC10b samples has an inefficiency due to a bug. The MC samples have lower efficiency than for high muon p_T. Therefore, the trigger cut itself is not used for MC and instead, the trigger efficiency taken directly from data is used [29] .

- **Vertex requirement**: To reject the non-collision background, the first offline-reconstructed primary vertex of the event must have at least five tracks.
- **Cosmic rejection**: The event is removed if it is identified to have cosmic muons, as described in Section 4.4.1.
- **Electron and muon overlap removal**: If the selected muon shared a track with an electron, the event is discarded.
- **Bad jet cleaning**: If any jet in the event with $p_T > 20$ GeV and positive energy fails the jet quality cuts which are designed to reject the bad jets (described in Section 4.4.2), the event is removed.
- $E_T^{\mathbf{miss}}$: Events must satisfy $E_T^{\text{miss}} > 40$ GeV.
- **Muon multiplicity and charge**: Exactly two selected muons with the same electric charge are required.

  The muon multiplicity requirement is applied in two steps. As it can be seen from Table , first the presence of at least two muons in an event is checked. This provides a chance to study multi-lepton events. Then the requirement of exactly two muons is applied.
- **Low mass cut**: Since the MC samples for Z +jets production are generated with a cut on the invariant mass of leptons at $M_{ll} > 10$ GeV, a cut for the reconstructed dimuon mass is applied for both MC and data events, requiring $M_{\mu\mu} > 15$ GeV. This cut also removes the contamination of low mass resonances.
- Z **veto**: Another cut on the invariant mass of dimuon is applied, requiring $|M_{\mu\mu} - m_Z| > 10$GeV, to reduce the background contamination from Z production.
- **Reconstruction truth**: This is a specific cut for MC. The most important background contributions to the same-sign dimuon events are from the mis-reconstructed muons. The data-driven background estimation is used for the muon mis-reconstruction. But the events with mis-reconstructed muons also exist in the MC samples. The mis-reconstructed events must be removed from MC to avoid double counting. This overlap is removed by requiring the reconstructed muons in the MC samples must be originated from a W leptonic decay (or subsequent τ decay). This is done by checking the ΔR between a reconstructed muon and a true muon and requiring $\Delta R < 0.2$.
- **Jets requirement**: Events must contain at least two selected jets. furthermore, event must have at least one b-tagged jet.

cut	fake BG	eff.(%)	other BG	eff.(%)	$t_R t_R$	eff.(%)	$tt\ m_{Z'} = 200$	eff.(%)
Before cuts	746.63	-	21007600.0	-	3637.71	-	126.84	-
Trigger	-	-	20898282.0	99.5	3595.14	98.8	124.60	98.2
Vertex cut	-	-	20512468.0	98.2	3578.28	99.5	124.19	99.7
# $\mu > 2$	-	-	681820.25	3.3	79.91	2.2	4.67	3.8
Bad jet clean	-	-	677933.94	99.4	73.99	92.6	4.52	96.8
E_T^{mis}	34.62	4.6	1198.11	0.2	50.11	67.7	2.51	55.4
# jets > 2	32.62	94.2	694.72	58	36.54	72.9	1.82	72.4
# $\mu = 2$	-	-	687.36	98.9	36.54	100	1.82	100
same-sign	5.39	16.5	4.49	0.7	36.54	100	1.82	100
$M_{\mu\mu} > 15$	5.39	100	4.49	99.9	36.54	100	1.82	100
Z veto	1.00	18.5	4.00	89.1	35.05	95.9	1.63	89.5
Reco. truth	-	-	2.93	73.2	35.05	100	1.63	100
# b-jets > 1	1.00	100	0.67	22.9	33.63	96.0	1.45	89.4

Table 4.2: Cut flows and cut efficiencies for background and two of signal samples. The fake background is the background due to the mis-reconstructed muons and is estimated from data. The data-driven sample which is used for this background estimation (see Section 5.2) is made for dilepton studies and the events in this sample are already passed some of the event selections such as trigger, vertex requirement, muon multiplicity requirement and event cleaning cut, before they enter the sample. For the other backgrounds the MC samples are used. Estimations from MC are scaled to the integrated luminosity of 2.05 fb^{-1}. The cut efficiency shows the percentage of number of events which survived from the cut.

Chapter 5

Background Estimation

The background processes for the same-sign top pair production can be divided to:

- SM processes with the same-sign prompt muon pairs
- SM processes with one or two non-prompt mis-reconstructed muons (*fake muons*)
- SM processes with opposite-sign muons where the charge of one of the muons is mis-measured (*charge mis-identification*)

These sources of background and the methods used to estimate them are described in detail in the following sections.

5.1 Prompt Same-sign Dileptons in the Standard Model

The prompt leptons are the muons or electrons originated from the decay of W and Z bosons or the subsequent tau leptons. There are several Standard Model processes leading to two high-p_T prompt leptons with the same electric charge in the final state.

One of these processes is the $W^{\pm}W^{\pm}$ production with associated jets, when both W bosons decay leptonically, i.e. $W^{\pm}W^{\pm} \rightarrow l^{\pm}\nu\ l^{\pm}\nu\ + jets$. The $W^{\pm}W^{\pm}$ pair can be produced in different ways, for example via t-channel exchange of a gluon or in a $q\bar{q}$ annihilation where one of the W bosons is radiated from an initial quark and the other one from a final quark, but it is always produced with two additional jets (in contrast to the $W^{+}W^{-}$ diboson production). The corresponding Feynman diagrams are shown in Figure 5.1.

The ZZ and WZ diboson productions can lead to two prompt same-sign leptons, via $ZZ \rightarrow l^{\pm}l^{\mp}\ l^{\pm}l^{\mp}$ and $WZ \rightarrow l^{\pm}\nu\ l^{\pm}l^{\mp}$. Also, the associated production of vector bosons with a $t\bar{t}$ pair, i.e. $t\bar{t}W$, $t\bar{t}Z$ and $t\bar{t}WW$, can give rise to prompt same-sign dilepton production.

The contribution of these processes to the signal selection region is estimated from MC simulation. The list of the MC samples which are used and the cross section of the corresponding processes are provided in Appendix B. The number of selected events after applying all selection cuts are available in Table 6.1. The dominant contribution of prompt same-sign dimuon background is from $t\bar{t}W$ and $W^{\pm}W^{\pm}$ $+2jets$.

5.2 Mis-Reconstructed Muons

The non-prompt muons, which are originated from the semi-leptonic decays of b- or c-hadrons or decay-in-flight of pion or kaon mesons, can be wrongly mis-reconstructed as prompt muons. The mis-reconstruction can also happen when a muon from a hadronic shower in the calorimeter reaches the

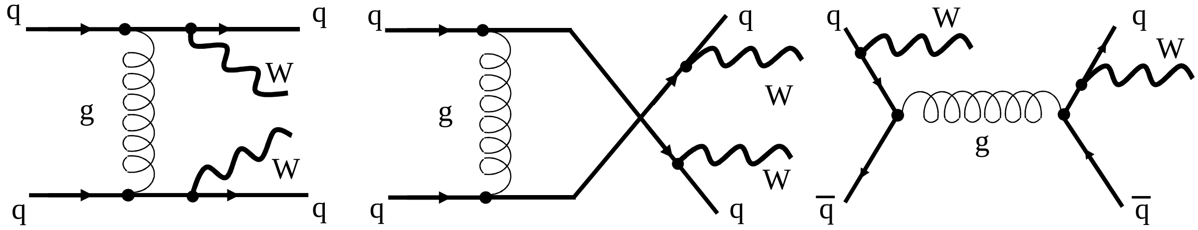

Figure 5.1: Feynman diagrams of $W^{\pm}W^{\pm}$ +2jets production in a hadron collider via gluon exchange

muon spectrometer and is wrongly matched to a reconstructed inner detector track. These non-prompt and mis-reconstructed muons are referred to as *fake* muons in this study.

The W boson production in association with jets, single-lepton decay of $t\bar{t}$ [1] and QCD multi-jets events contribute in the signal selection due to the fake muons. The predominant contribution is from W +jets and single-lepton decay of $t\bar{t}$ where one muon is real and comes from the W decay and the other muon is fake and is originated from one of the jets. The smaller contribution is from the QCD multi-jets production where both muons are fake.

It is most appropriate to estimate the background due to the fake muons from the data-driven methods because this background is poorly modeled in MC simulation. The result of the data-driven technique called the *matrix method* is used in this study [9] . The method is based on selecting two sets of leptons, *loose* (L) and *tight* (T), and determining the probabilities that are called *fake* and *real* rates (f and r).

The tight muons pass the tight selection criteria which is identical to the muon selection described in Section 4.4.1. The loose muons fulfill the same selection criteria without the isolation requirement. The fake rate is defined as the probability that a loose fake muon passes the tight selection and the real rate is the probability that a loose prompt muon is selected as a tight muon. The real and fake rates are measured from data, using purified control regions.

A sample of opposite-sign dimuon events with the invariant mass compatible with the Z boson mass, is dominated by real muons coming from Z boson decay. From this control sample r is measured for different p_T and η ranges. The fake-enhanced control sample is provided by selecting events with

---

[1] One of the W bosons originated from the top or antitop quark decays leptonically and the other one hadronically.

exactly one muon, at least one jet (with $p_T > 20$ GeV), low E_T^{miss}, ΔR (*leading jet*, μ) > 0.7 and no overlap removal between muon and jets. This control region is used for measuring f for the same p_T and η ranges [9] .

A dimuon event that passes the event selection without requiring the muon isolation cuts (a pre-isolated dimuon event), contains two loose muons or a loose and a tight muon or two tight muons. The number of these events are labeled by N_{LL}, N_{TL}, N_{LT} and N_{TT}, depending on tightness or looseness of the leading (first index) and sub-leading (second index) muons. These quantities along with f and r are the inputs of the matrix method. One can calculate the number of dimuon events in terms of the composition of real and fake muons from the following matrix equation:

$$\begin{bmatrix} N_{TT} \\ N_{TL} \\ N_{LT} \\ N_{LL} \end{bmatrix} = \begin{bmatrix} r_1 r_2 & r_1 f_2 & f_1 r_2 & f_1 f_2 \\ r_1(1-r_2) & r_1(1-f_2) & f_1(1-r_2) & f_1(1-f_2) \\ (1-r_1)r_2 & (1-r_1)f_2 & (1-f_1)r_2 & (1-f_1)f_2 \\ (1-r_1)(1-r_2) & (1-r_1)(1-f_2) & (1-f_1)(1-r_2) & (1-f_1)(1-f_2) \end{bmatrix} \begin{bmatrix} N^{ll}_{RR} \\ N^{ll}_{RF} \\ N^{ll}_{FR} \\ N^{ll}_{FF} \end{bmatrix} \tag{5.1}$$

where the $N^{ll}_{R(F)R(F)}$ is the number of loose events containing a real (fake) leading muon and a real (fake) sub-leading muon. The matrix can be inverted to solve the equation for N^{ll}_{RF}, N^{ll}_{FR} and N^{ll}_{FF}. Then one can obtain the number of events with at least one fake muon in the signal region, i.e. the region with two tight muons:

$$N^{tt}_{RF} = r_1 f_2 N^{ll}_{RF}\,, \qquad N^{tt}_{FR} = f_1 r_2 N^{ll}_{FR}\,, \qquad N^{tt}_{FF} = f_1 f_2 N^{ll}_{FF} \tag{5.2}$$

and the sum of these three components gives the total contribution of fake background:

$$N_{fake} = N^{tt}_{RF} + N^{tt}_{FR} + N^{tt}_{FF} \tag{5.3}$$

A data-driven sample of fake events estimated by the matrix method is provided by the reconstruction group of top working group of ATLAS. This sample is used to estimate the contribution of fake events in the background and its uncertainty. The fake background is estimated in data corresponding to 0.7 fb^{-1} integrated luminosity. The sample of obtained distributions is weighted to 2 fb^{-1}. The result of this background estimation is in Table 6.1.

5.3 Charge Mis-Identification

Standard Model processes with an opposite-sign muon pair in the final state may contribute to the background if the charge of one of the muons is mis-identified.

The source of charge mis-identification for muons is the mis-reconstruction of the track curvature. In the inner detector, it is most likely to happen at high momenta, where the track has a lower curvature. But the curvature measurement for muons is the combination of measurements in the inner detector (ID) and the muon spectrometer (MS). For high p_T muons, the low curvature of ID track is compensated with the MS measurement. In the muon selection, the requirement of agreement between the sign of charges measured in the ID and MS subsystems (see Section 4.4.1), reduces the background caused by the muon charge mis-identification to a negligible rate.

The invariant mass distributions of the same- and opposite-sign dimuon events are presented in Figure 5.2. The events are selected by removing the cuts on E_T^{miss} and jet multiplicity from the event selection in Section 4.4.4 and requiring an invariant mass of $|M_{\mu\mu} - 91| < 10$ GeV. This region is enhanced by real opposite-sign dimuons which are originated from Z boson decays. A *same*-sign dimuon originated from a Z boson decay is resulted from charge mis-identification of the muons. As it can be seen in Figure 5.2b, the distribution of same-sign events in data is very flat. The same distribution from the MC simulation shows very few events. Without a peak structure around the Z boson mass, it cannot be indicated that the muons are originated from Z boson and the same-sign dimuon events could be arisen from fake muons. Considering the distributions in 5.2b, one expects the rate of charge mis-identification to be very small.

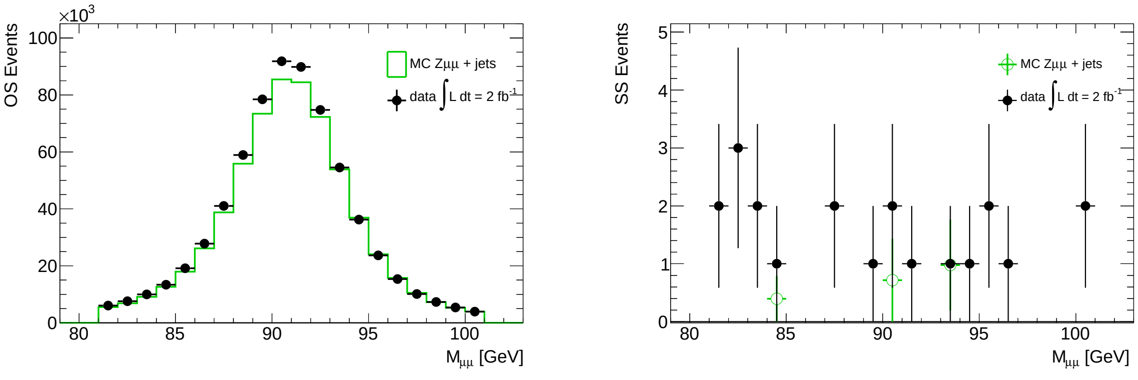

(a) Opposite-sign

(b) Same-sign

Figure 5.2: The invariant mass distribution for same- and opposite-sign dimuon events around the Z mass. MC samples are normalized to 2 fb^{-1}integrated luminosity.

By applying the $Q_{ID} = Q_{MS}$ cut, a charge mis-identification can only happen if the curvature of *both* ID and MS tracks are mis-reconstructed. Therefore, the probability of such a mis-reconstruction or *charge flip* rate for both subsystems are measured separately and multiplied together to get the probability of muon charge mis-identification.

The charge flip rate is directly estimated from data. To probe the ID (MS) charge measurement, the MS (ID) is used as a reference subsystem . After removing the requirement of $Q_{ID} = Q_{MS}$ in the muon selection, the candidates of $Z \rightarrow \mu^+\mu^-$ events are selected based only on the MS (ID) measurement. The Z candidates are selected by requiring two muons with the opposite MS (ID) charges and an invariant mass in the range $76 < M_{\mu\mu} < 106$ GeV which is reconstructed from the MS (ID) momentum. The invariant mass distributions are shown in Figure 5.3. Then for the muons in the selected Z candidate events, the charge measured by the probing subsystem is compared with the charge measured by the reference subsystem. The ID (MS) charge flip rate is the ratio of the number of muons with non-consistent ID and MS charge, to the number of all muons found in the sample of Z events selected by MS (ID) measurement. The rates are measured as a function of p_T and η.

The result of this measurement is shown in Figure 5.4 for the MS. The MS charge flip rate in data increases from 10^{-3} for $p_T < 50$ GeV to almost 10^{-1} for $200 < p_T < 250$ GeV. As a function of η, it shows an increase in the region of $1.2 < |\eta| < 1.6$. This corresponds to the transition region between the different MS sections and the ATLAS magnetic system (see Section 3.2.3).

For the ID, on the other hand, the charge flip rate is measured to be consist with zero. In both data and MC, no muon is found in the Z events selected by MS measurements which have non-consistent ID charge. The ID performance for the range of muon p_T explored in this research is very good.

Since the ID charge flip rate is consist with zero and the global muon charge flip rate is the product

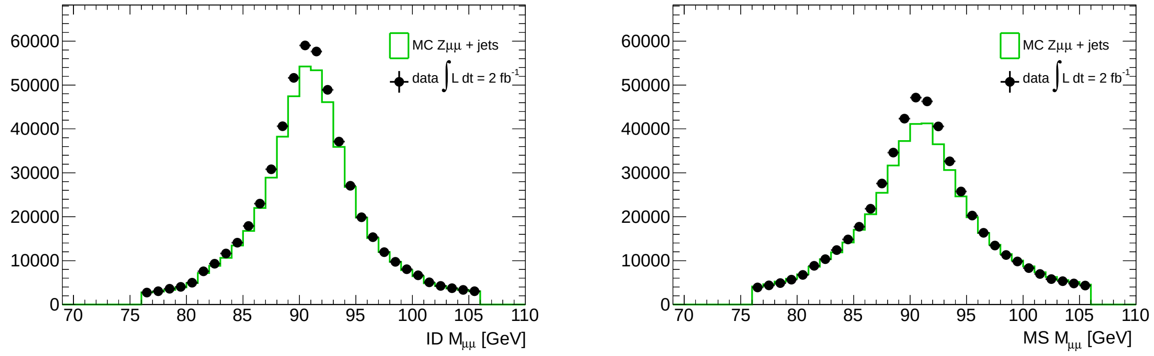

(a) based on ID

(b) based on MS

Figure 5.3: The invariant mass distribution of opposite-sign dimuon events around the Z mass, based only on one of the subsystems measurements. MC samples are normalized to 2 fb^{-1}integrated luminosity.

of charge flip rates of the two subsystems, the muon charge flip has a negligible rate according to the data-driven estimation. The MC samples of processes with opposite-sign dimuon are used to predict the background contribution due to the muon charge mis-identification. After applying all the selection cuts, the contribution of $t\bar{t}$, single top, $Z \to \mu\mu$ and $Z \to \tau\tau$ are less than 3 events, considering the statistical fluctuation, and the contribution of W^+W^- is very small. The final event yields are available in Table 6.1.

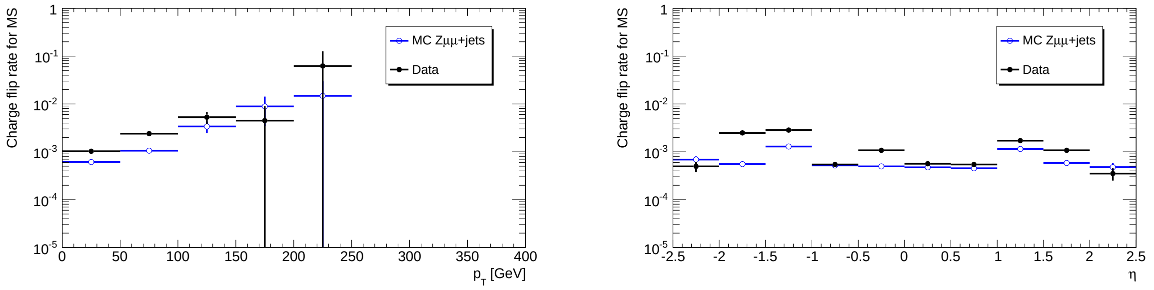

(a) as a function of p_T

(b) as a function of η

Figure 5.4: Charge flip rate for MS.

Chapter 6

Results

6.1 Control Region

The control selecting region is used to validate the basic performance of muons, missing transverse energy and jets and the modeled efficiencies and acceptances . This is done by comparing the Standard model expectations with data in the opposite-sign dimuon control region which is dominated by $t\bar{t}$ decays.

The control sample is selected by applying the same selection cuts of the Section 4.4.4, except that the same-sign requirement for muons is changed to opposite-sign. The SM expectation is derived from MC simulation for $t\bar{t}$ events, data-driven sample for fake background and MC simulation for all the other background.

The comparison between the Standard model expectations and data is illustrated in Figures 6.1 to 6.4. The uncertainties illustrated in the plots are the combination of systematic and statistical uncertainties for the SM expectations (with considering the correlations) and statistical uncertainty for data. Contribution from ZZ , ZW and W^+W^- productions in background are summarized as ‘ diboson ′ while the $W^\pm W^\pm + 2jets$ production and the associated production of vector bosons with $t\bar{t}$ pair are grouped together. The data is consistent with SM expectations within the uncertainties[1].

---

[1] The event yields are compared with other groups who are working on $t\bar{t}$ dilepton decays at ATLAS and the numbers agree.

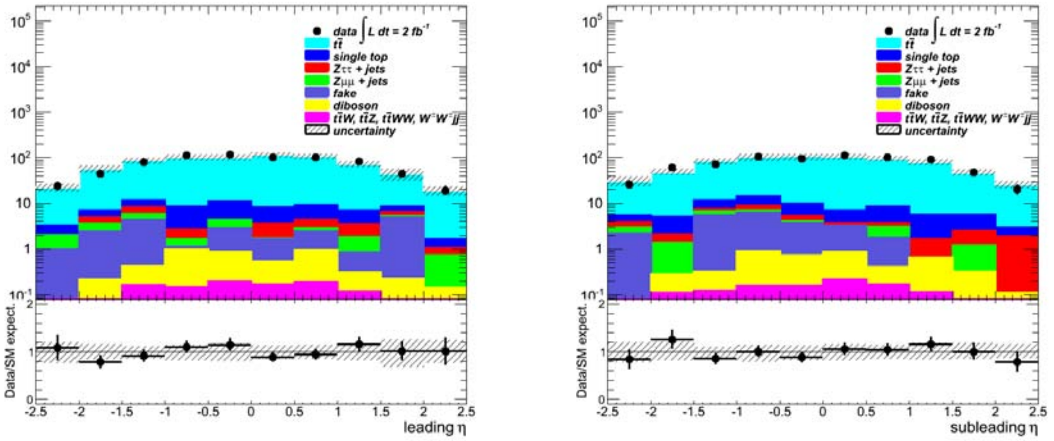

(a) leading muon η

(b) subleading muon η

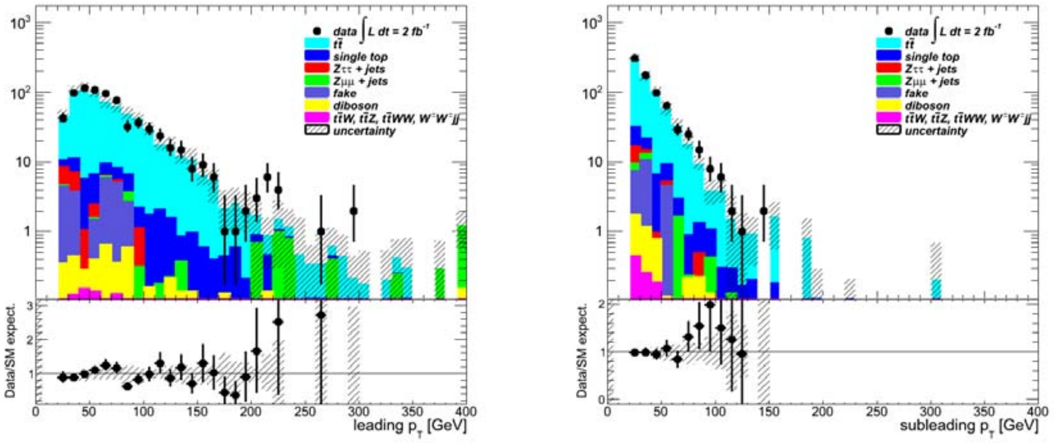

(c) leading muon p_T

(d) subleading muon p_T

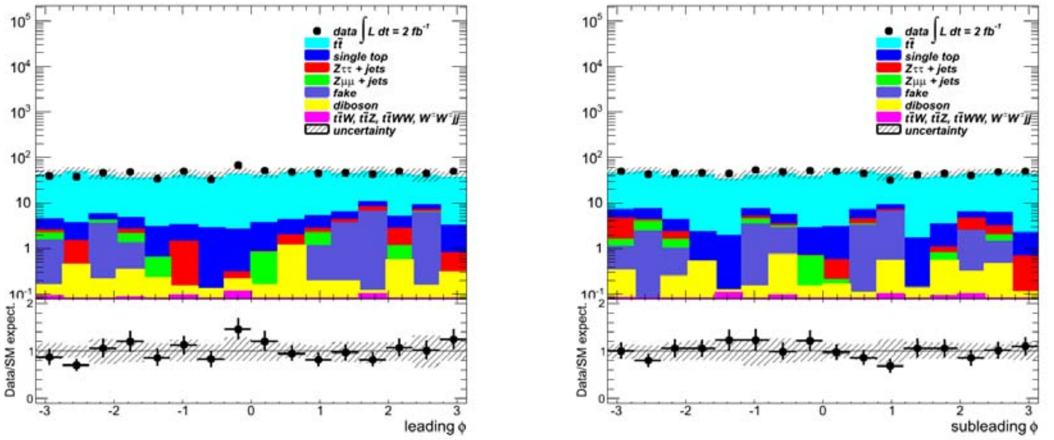

(e) leading muon φ

(f) subleading muon φ

Figure 6.1: Distribution of muons pseudorapidity (top) transverse momentum (middle) and azimuthal angle (bottom) for leading (left) and subleading (right) muons in opposite-sign dimuon control region.

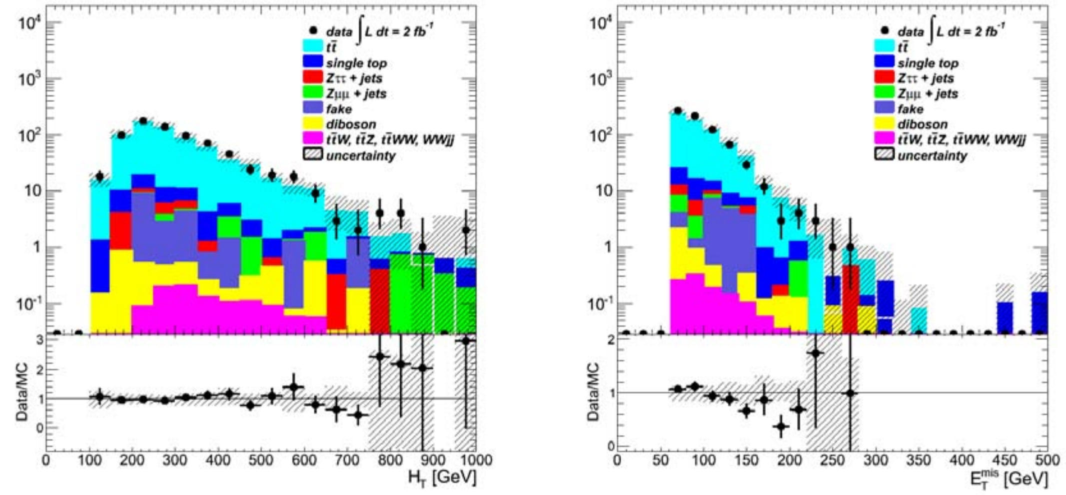

(a) H_T

(b) E_T^{miss}

Figure 6.2: Distribution of H_T (left) and missing transverse energy (right) in opposite-sign dimuon control region. H_T is defined as the scalar some of p_T of selected leptons and jets in the event. (Note: The correct label of y-axis in the ratio plot is Data/SM expectation.)

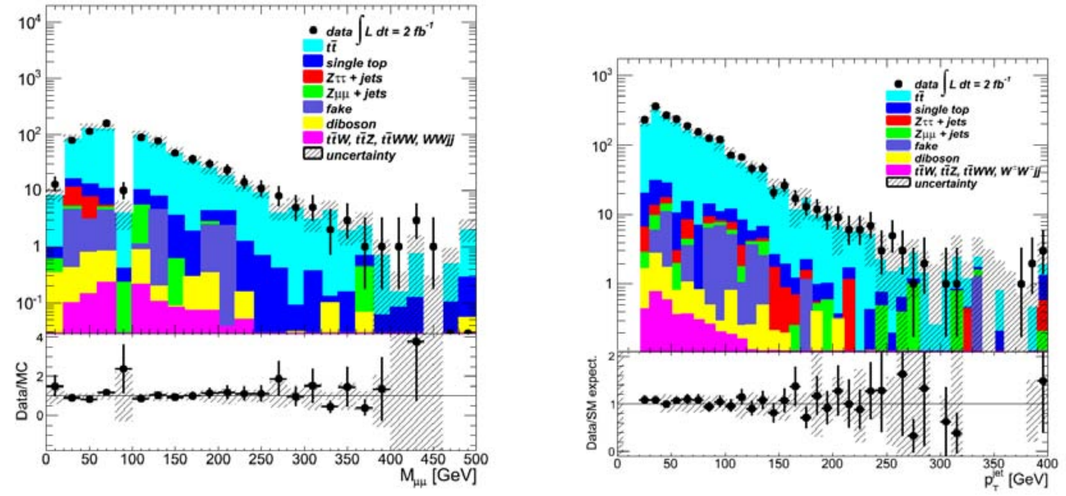

(a) $M_{\mu\mu}$

(b) p_T^{jet}

Figure 6.3: Distribution of dimuon invariant mass (left) and jet transverse momentum (right) in opposite-sign dimuon control region. (Note: The correct label of y-axis in the ratio plot is Data/SM expectation.)

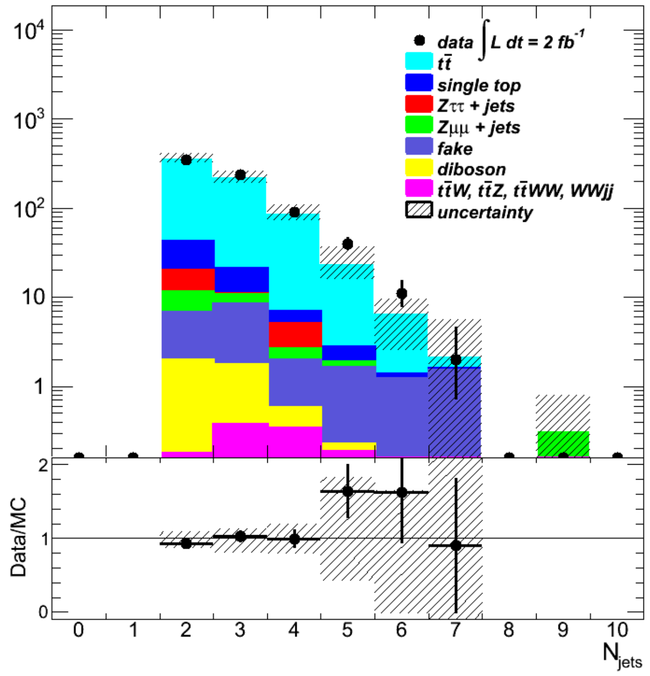

Figure 6.4: Distribution of jet multiplicity in opposite-sign dimuon control region. (Note: The correct label of y-axis in the ratio plot is Data/SM expectation.)

6.2 Signal Region

The expected and measured number of events in the signal region after applying all the selection cuts (described in Section 4.4.4) are shown in Table 6.1. In a data set of 2 fb^{-1}of integrated luminosity, 5 events are observed. The number of expected background events in total is estimated from MC simulation and data-driven methods to be $1.7\ ^{+3.2}_{-1.0}(stat.)\ ^{+0.1}_{-0.4}(syst.)$. The observed number of events in data is consistent with expected SM background within the uncertainties, so there is no evidence of new physics. The result of the counting experiment is used to set limits for various models. (It will be describe in Section 6.4.)

The estimation shows that 60% of the background is due to the mis-reconstructed muons, 35% due to the prompt same-sign dimuon events and 5% from muon charge mis-identification.

The results of the signal selection region are also shown in Figures 6.5 to 6.7 . The uncertainties illustrated in the plots are the combination of systematic and statistical uncertainties for the background events (with considering the correlations) and statistical uncertainty for data. Contribution from ZZ , ZW and W^+W^- productions in background are summarized as ‘ diboson ′ while the $W^{\pm}W^{\pm} + 2jets$ production and the associated production of vector bosons with $t\bar{t}$ pair are grouped together.

Process	Number of events
single top	$0\,^{+3}_{-0}\,\pm 0$
$t\bar{t}$	$0\,^{+3}_{-0}\,\pm 0$
$Z \to \tau\tau$ +jets	$0\,^{+3}_{-0}\,\pm 0$
$Z \to \mu\mu$ +jets	$0\,^{+3}_{-0}\,\pm 0$
W^+W^-	$0.09\,^{+1.89}_{-0.09}\,^{+0.02}_{-0.03}$
ZZ	$0.040\,^{+1.862}_{-0.037}\,^{+0.004}_{-0.006}$
WZ	$0.01\,^{+1.85}_{-0.01}\,^{+0.05}_{-0.14}$
$W^\pm W^\pm$ +2jets	$0.14\,^{+1.92}_{-0.14}\,^{+0.02}_{-0.03}$
$t\bar{t}W$	$0.36\,^{+2.03}_{-0.04}\,^{+0.05}_{-0.08}$
$t\bar{t}W$ +jet	$0.017\,^{+1.851}_{-0.017}\,^{+0.002}_{-0.005}$
$t\bar{t}Z$	$0.0033\,^{+1.8429}_{-0.0033}\,^{+0.0003}_{-0.0011}$
$t\bar{t}Z$ +jet	$0.0029\,^{+1.8427}_{-0.0029}\,^{+0.0003}_{-0.0008}$
$t\bar{t}WW$	$0.0044\,^{+1.8435}_{-0.0044}\,^{+0.0005}_{-0.0010}$
fakes	$1.0\,^{+2.3}_{-0.8}\,^{+0}_{-0.3}$
Total background	$1.7\,^{+3.2}_{-1.0}\,^{+0.1}_{-0.4}$
Data	5
$t_R t_R$	$33.6 \pm 5.8\,^{+3.2}_{-7.6}$
$t_L t_L$	$34.0 \pm 5.8\,^{+0.1}_{-8.3}$
$t_L t_R$	$4.8\,^{+3.3}_{-2.1}\,^{+0.1}_{-1.2}$
$tt\ m_{Z'}$ = 200 GeV	$1.5\,^{+2.5}_{-1.1}\,^{+0.2}_{-0.3}$
$tt\ m_{Z'}$ = 150 GeV	$0.8\,^{+2.2}_{-0.7}\,^{+0.1}_{-0.2}$
$tt\ m_{Z'}$ = 100 GeV	$0.340\,^{+2.019}_{-0.337}\,^{+0.036}_{-0.071}$

Table 6.1: Final event yields, after all selection cuts. The numbers are reported in the form of $N \pm \Delta N_{statistic} \pm \Delta N_{systematic}$.

6.3 Systematics Uncertainty

The results of the analysis are affected by systematic uncertainties as well as statistical uncertainties. Statistical uncertainties are due to the random fluctuations arising from the fact that a measurement is based on a finite set of observations. Systematic uncertainties, on the other hand, arise from uncertainties associated with the nature of the measurement apparatus, assumptions made by the experimenter, or the model used to make inferences based on the observed data[40].

To estimate the effect of the systematic uncertainties on the result of the analysis, the quantities asso-

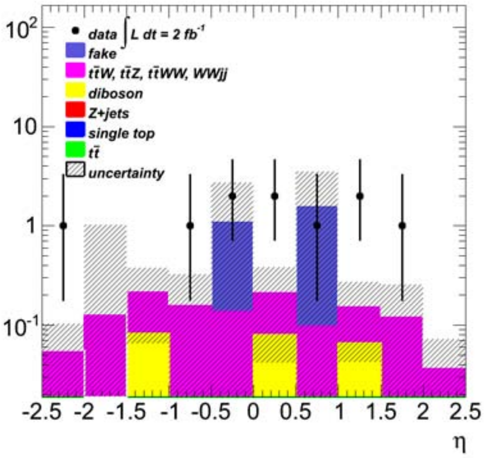

(a) muon η

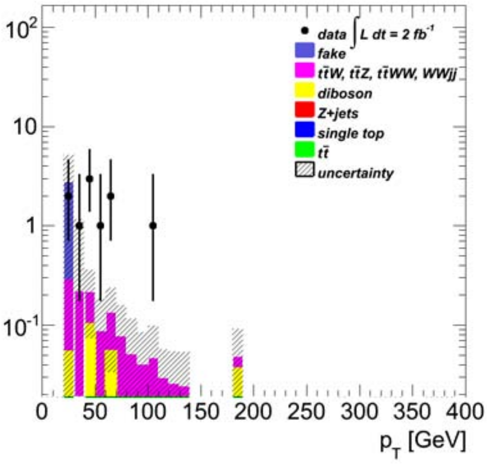

(b) muon p_T

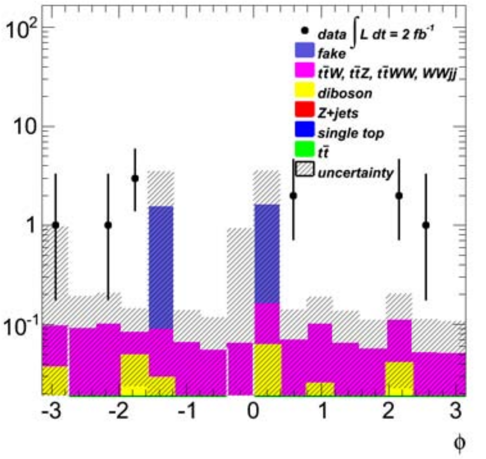

(c) muon φ

Figure 6.5: Distribution of muons pseudorapidity (top) transverse momentum (middle) and azimuthal angle (bottom) in the signal region.

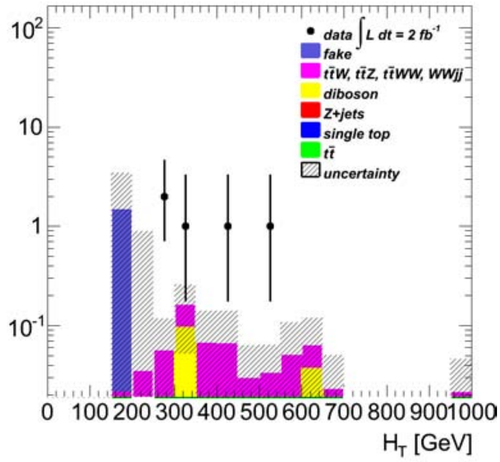

(a) H_T

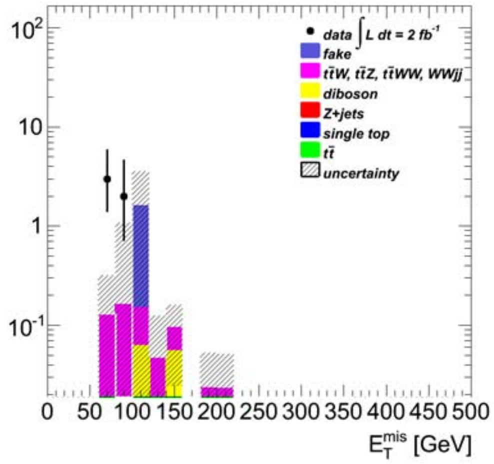

(b) E_T^{miss}

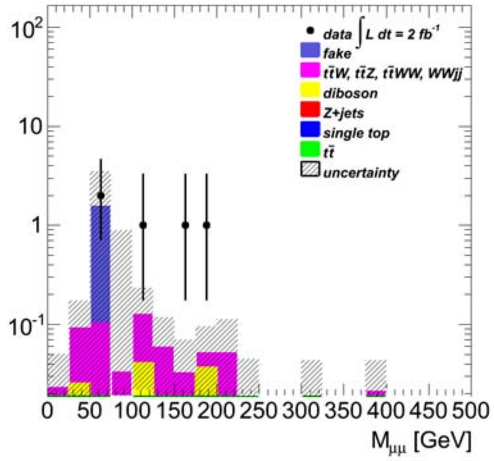

(c) $M_{\mu\mu}$

Figure 6.6: Distribution of H_T (top), missing transverse energy (middle) and dimuon invariant mass (bottom) in the signal region. H_T is defined as the scalar some of p_T of selected leptons and jets in the event.

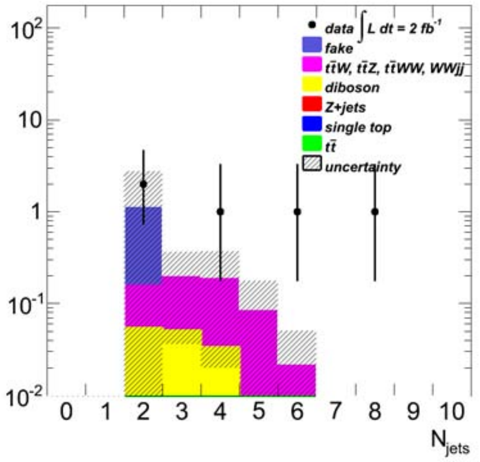

(a) N_{jets}

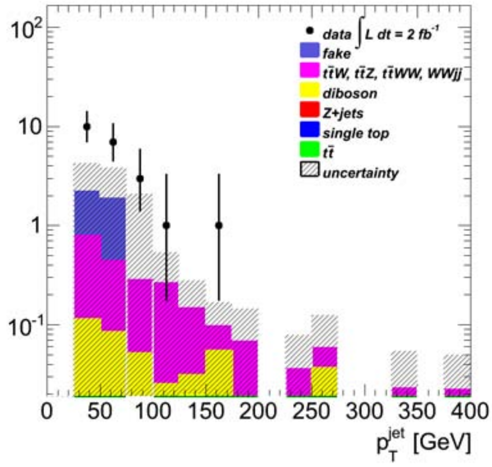

(b) p_T^{jet}

Figure 6.7: Distribution of jet multiplicity (top) and jet transverse momentum (bottom) in the signal region.

ciated with deferent sources of the systematics are varied in the MC samples of signal and background, usually by one scale up and down. Then the full analysis is repeated and the number of events after all selection cuts are counted. The differences with the nominal analysis are quoted as systematic errors.

There are different sources for systematic uncertainties associated with objects (jets, muons and E_T^{miss}), data-driven method for background estimation, luminosity and theoretical cross sections for MC simulated background. For estimating the systematic uncertainties, the recommendations of ATLAS top working group is followed [31]. Each systematic source that is used in this analysis is described below. The result of systematic estimation is summarized in Table 6.2.

Jets

Reconstructed jets are calibrated to the energy scale measured by the electromagnetic and hadron calorimeters. The uncertainties on jet energy scale (JES) calibration is one of the largest source of systematic uncertainty in this analyses. The JES uncertainty is derived by using the information from test-beam data, LHC collision data and simulation and depends on jet p_T and η [42]. The MultijetJESUncertaintyProvider tool [33] of the ATLAS collaboration, provides the JES uncertainty values for individual jets as a function of jet p_T and η. The momentum and energy of individual jets in the corresponding MC samples were rescaled by the values of one standard deviation upward and downward, to estimate the JES uncertainty and as described above.

Jet energy resolution (JER) is the resolution of the reconstructed jet p_T and its value, σ_{p_T}, is measured from data-driven methods along with its uncertainty. The jet p_T in MC samples are smeared according to a Gaussian with the width of σ_{p_T} to match with data. To estimate the uncertainty due to JER, the MC samples are smeared with the value of $\sqrt{(\sigma_{p_T} + \Delta\sigma_{p_T})^2 - \sigma_{p_T}^2}$ where $\Delta\sigma_{p_T}$ is the resolution uncertainty from data-driven method and the difference of the analysis result with respect to the result obtained from nominal MC is considered as the systematic uncertainty. The corresponding tool is provided by ATLAS collaboration [15].

The limited efficiency of the jet reconstruction algorithm is another systematic uncertainty source. Jet reconstruction efficiency (JRE) is measured by matching calorimeter jets to track jet as a function of jet p_T and η. Jets are randomly removed from the events (about 2%of jets) and the difference of results with respect to nominal samples are considered as the uncertainty. The contribution of JRE in the systematic uncertainty in this analysis is very small.

The uncertainties from JES, JER and JRE are propagated to E_T^{miss}, since according to Equation 4.1 they affect the E_T^{miss} calculation.

Muons

The efficiency of muon reconstruction, identification and trigger are determined from candidate $Z \to \mu\mu$ with the so called tag and prob method. The ratios of the efficiencies of data to MC are the scale factors (SF) which used to re-weight the events in MC. To get the corresponding uncertainties, events were re-weighted with upward and downward values of scale factors. The uncertainty corresponding to muon trigger efficiency SF is the dominant systematic uncertainty in this analysis while the contribution of muon reconstruction+identification efficiency SF in the systematic uncertainty is high too.

Muons energy scale and energy resolution (ER) also have uncertainties that affect the result. Similar to the jets, the muon p_T in the MC simulation is smeared and corrected until it can reproduced the Z peak in decay to muons in the same invariant mass value and with the same width which are observed in data. The smearing parameters for ID and MS momenta are varied upward and downward separately.

The highest and the lowest value of result among the four values obtained after smearing with these new parameters has been averaged to quote as the systematic uncertainty.

The effect of these systematic uncertainties are propagated to E_T^{miss} as well, for the same reason discussed for jets.

E_T^{miss}

The missing transverse energy is calculated from Equations 4.1 and 4.2, so every systematic uncertainty of other objects arise from energy scale, energy resolution and object reconstruction and identification affects it. As it mentioned before, the propagation of these uncertainties to E_T^{miss} is considered. The cell-out term of equation includes all the energy deposit in calorimeter which is not related to any of reconstructed objects. The uncertainty of this term should be considered as well. The soft jets contribution in E_T^{miss} is correlated with cell-out term, so their uncertainties are computed together. Also, the pile-up effect and the liquid Argon (LAr) hole problem[2] affect the E_T^{miss} calculation and their contribution to E_T^{miss} uncertainty are considered too. The estimated systematic uncertainties of E_T^{miss} in this analysis are very small.

Data-driven fake estimation

Uncertainty due to the fake background estimate from data-driven method (described in Section 5.2) is estimated by varying the data-driven sample with the upward and downward weights that are already provided in the sample. The weights are derived from the difference in the observed and predicted number of fake events in certain control regions.

Other sources

There are other systematic uncertainty sources which are included in the plots of signal and control region(Figures 6.1 to 6.7) but they are not included in Table 6.2. The uncertainty on the measured integrated luminosity is considered 4%. The uncertainty on the theoretical cross sections used for the MC simulation are considered as: 5% for dibosons (ZZ , ZW , W^+W^-), 10% for single top, 10% for $t\bar{t}$, 4% for Z and 100% for $t\bar{t}W/Z/WW$ and $W^\pm W^\pm + 2jets$.

---

[2] On April 30th 2011, 6 of the front end boards of the ATLAS liquid Argon calorimeter were lost due to some technical problems. This failure occurred after the production of the MC10 samples and it is required to be fixed at the analysis level [28].

$\Delta N/N(\%)$ Syst. Source	total BG	$t_R t_R$	$t_L t_L$	$t_L t_R$	$tt\ m_{Z'} = 100$	$tt\ m_{Z'} = 150$	$tt\ m_{Z'} = 200$
JES	$+0/-19$	$+0/-0.6$	$+3/-0$	$+2/-1$	$+5/-9$	$+7/-5$	$+4/-6$
JER	±10	±0.9	±0.6	±9	±0.4	±0.3	±0.9
JRE	±0	±0	±0	±0.3	±0	±0.1	±0
μ ER	±0.4	±0.2	±0.1	±0.3	±1	±0.4	±0.4
μ trigger eff. SF	$+3/-23$	$+3/-21$	$+3/-23$	$+3/-21$	$+2/-17$	$+2/-17$	$+3/-20$
μ reco.+id. eff. SF	±9	$+9/-8$	$+9/-8$	$+9/-8$	$+9/-8$	$+9/-8$	$+9/-8$
E_T^{miss} cell-out	$+0.3/-0$	$+0.9/-0.6$	$+0/-0.4$	$+0/-0.5$	$+0.6/-1$	$+0.8/-0.2$	$+0.3/-0.4$
E_T^{miss} LAr cleaning	$+0.7/-0.2$	$+1/-0$	$+0/-0.5$	$+0/-0.2$	$+0.2/-0.6$	$+0.4/-0$	$+0.2/-0.5$
E_T^{miss} pile-up	$+0.3/-0$	$+0.5/-0.6$	$+0.5/-0$	$+0.03/-0.6$	$+0/-1$	$+1/-0.1$	$+0.6/-0.3$
Data-driven	$+0/-32$	-	-	-	-	-	-
Total systematic uncertainty	$+6/-23$	$+10/-23$	$+0.3/-24$	$+2/-24$	$+10/-21$	$+12/-20$	$+11/-22$

Table 6.2: Systematic uncertainties on background estimation and expected number of signal events from different systematic sources. The uncertainties are presented as $\Delta N_{syst.}/N$ in percentage.

6.4 Limit Setting

In the searching experiments for new physics, the quantitative interpretation of the analysis result is the limit that is set for the understudying hypothesis. The goal is making a statement about how compatible is the observed result with the predictions of new physics hypothesis.

In order to measure the agreement of the observation with the new physics hypothesis, the probability density function (p.d.f.) of a test statistics, X, is built for both background hypothesis and the hypothesis of simultaneous presence of new physics particles and background (signal+background). The test statistics should be defined appropriately in order to discriminate the signal-like outcomes from the background-like ones. Then one calculates the probability of observing a value of X equal or less than[3] X_{obs}, the value of test statistics for the observed results, for both background and signal+background hypothesis. This gives the Confidence Level (CL) of each hypothesis[35]:

$$CL_{s+b} = P_{s+b}(X \leqslant X_{obs}) \tag{6.1}$$

$$CL_b = P_b(X \leqslant X_{obs}) \tag{6.2}$$

Small values for CL_{s+b} mean that the observation is not in agreement with predicted signal very well, while a value of CL_b close to 1 denotes the background-like behavior. The value of $1 - CL_{s+b}$ can be used to quote the exclusion level of a new physics hypothesis. For values of $CL_{s+b} < 0.05$, the signal+background hypothesis can be excluded with 95% CL.

As this analysis is based on cut and count method, the number of events is the observable used as the test statistics. The number of events, n, is expected to follow a Poisson distribution. So the p.d.f. for signal+background and background only hypothesis are:

$$P(n; s+b) = \frac{e^{-(s+b)}\,(s+b)^n}{n!} \tag{6.3}$$

$$P(n; b) = \frac{e^{-b}\,b^n}{n!} \tag{6.4}$$

where s is the expected number of signal events, obtained from MC, and b is the expected number of background events, obtained from MC and data-driven methods. By summing the p.d.f. in Equations 6.3 and 6.4 over the number of events up to the the observed number of events in data, n_{obs}, one obtains the CL_{s+b} and CL_b.

But the problem is the $s + b$ and b are affected by systematic errors. The true values of expected signal+background and expected background are distributed around the $s + b$ and b, according to a Gaussian distribution with the standard deviation equal to the systematic uncertainty.

In practice, to include the systematic uncertainties, a Gaussian random number generator with mean value of s (b) and standard deviation of $\Delta s_{syst.}$ ($\Delta b_{syst.}$) is used to get the expected number of signal (background) within the error range (the numbers are available in Table 6.1). Then these randomly generated numbers are used as the mean value of a Poisson random number generator, to create the distributions in Equations 6.3 and 6.4, where the systematic errors correlations are considered when needed. The resulted distributions are normalized to 1.

The p.d.f. of different signal models and background, built from this method, are shown in Figure 6.8. By integrating them up to the n_{obs}, the CL_{s+b} of different signal models and CL_b are calculated.

For the background, the calculated value is $CL_b = 0.98$. It can be seen that the expected background is compatible with the observed number of events in data. The values for CL_{s+b} are available in Table 6.3.

---

[3] The test statistics are usually defined to increase monotonically withe the number of events

The two signal models which predict the production of same-sign top quarks with identical helicity states from heavy mediators ($t_R t_R$ and $t_L t_L$), have small enough CL_{s+b} to exclude them with 99% CL. The rest of the signal models can not be excluded with the available statistics.

Signal sample	CL_{s+b}
$t_R t_R$	0.0001
$t_L t_L$	0.0003
$t_L t_R$	0.30
$tt\ m_{Z'}$ = 200GeV	0.61
$tt\ m_{Z'}$ = 150GeV	0.70
$tt\ m_{Z'}$ = 100GeV	0.95
Background	CL_b = 0.98

Table 6.3: CL_b and CL_{s+b}'s for all signal models

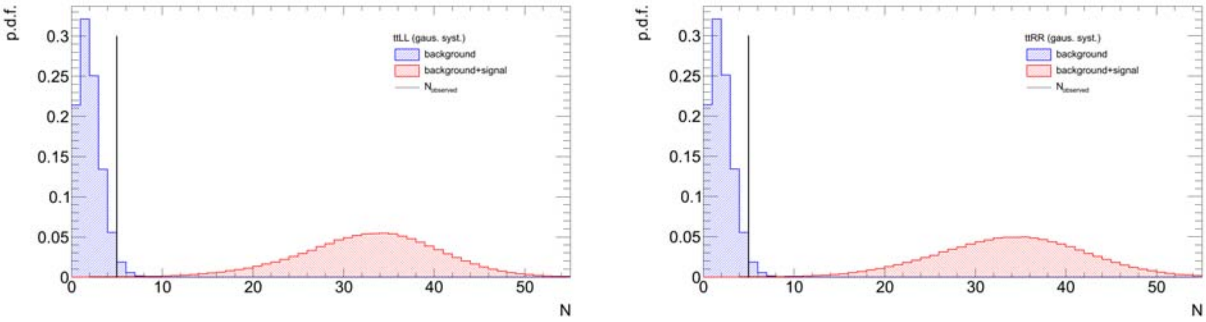

(a) $t_L t_L$

(b) $t_R t_R$

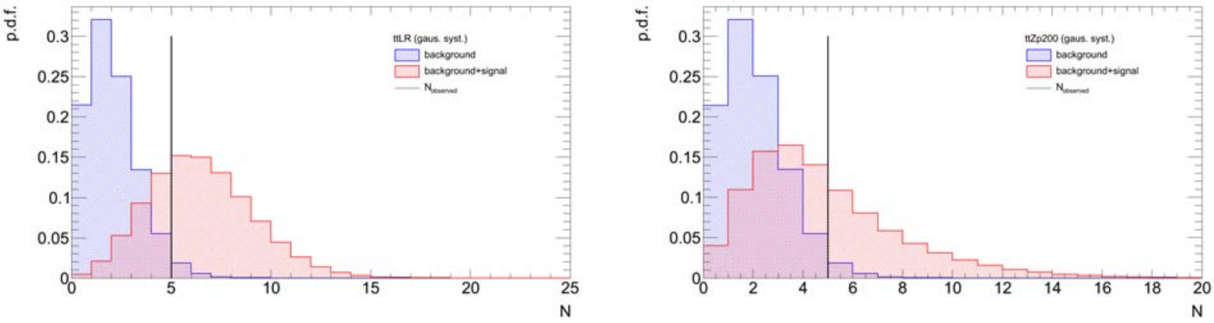

(c) $t_L t_R$

(d) $m_{Z'}$ = 200GeV

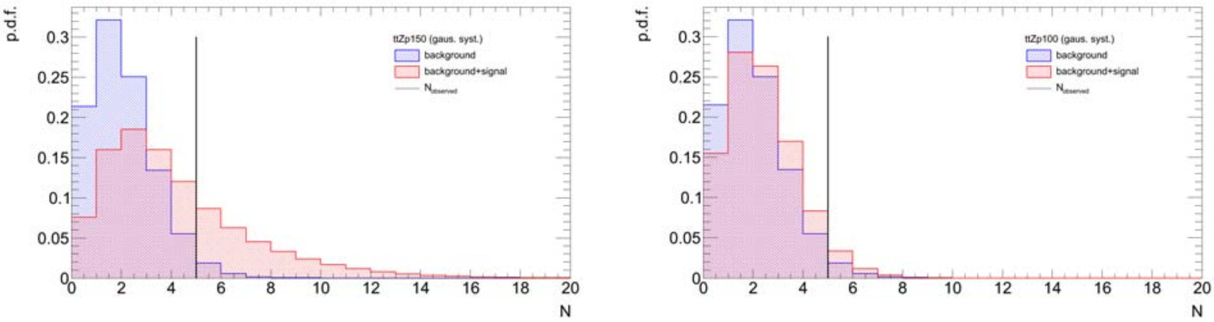

(e) $m_{Z'}$ = 150GeV

(f) $m_{Z'}$ = 100GeV

Figure 6.8: The distributions of probability density function for signal+background hypothesis (in red) and background only hypothesis (in blue) for different signal models. The black line shows the observed number of events in data. According to Equations 6.1 and 6.2, CL_{s+b} is obtained by integrating the red distribution up to N_{obs} and CL_b in a similar way, from the blue distribution.

Appendix A

Top Quark Forward-Backward Asymmetry

At Tevatron, which is a proton-antiproton collider, top quarks are predominately produced as $t\bar{t}$ pairs from quark-antiquark annihilations. Top quarks are observed to be produced preferentially in the forward region of rapidity[1] at Tevatron. The forward direction is defined by the direction of the incident proton beam. The forward-backward asymmetry is defined as

$$\mathrm{A_{FB}} = \frac{N(\Delta y > 0) - N(\Delta y < 0)}{N(\Delta y > 0) + N(\Delta y < 0)} \tag{A.1}$$

where $\Delta y = y_t - y_{\bar{t}}$ is the frame-invariant difference of the t and $\bar{t}$ rapidities in an event. In the Standard Model, this asymmetry arises from the higher order QCD contributions. But the measured value for forward-backward asymmetry shows a deviation from SM expectations. More interestingly, $\mathrm{A_{FB}}$ shows a mass dependency in addition to the rapidity dependency. It is observed to be more pronounced in the large $t\bar{t}$ invariant mass ($M_{t\bar{t}}$) region and in the region where Δy is large.

The published result of the CDF collaboration measurements with 5.3 fb^{-1}of data at $sqrts$=1.96 TeV shows a deviation of about two standard deviations (2σ) from the SM expectations and in the large $M_{t\bar{t}}$ region it increases to 3σ and more [18] . A more recent CDF measurement with 8.7 fb^{-1}of data (the full Tevatron dataset) shows that the rapidity and mass dependence of the asymmetry are well fit by linear functions, with a slope of $(15.6 \pm 5.5) \times 10^{-4}$ for $\mathrm{A_{FB}}(M_{t\bar{t}})$; to be compared with 3.3×10^{-4} from the next-to-leading-order SM expectation [19] .

---

[1] The definition of rapidity is $y = \frac{1}{2}\ln(\frac{E+p_z}{E-p_z})$. In the limit where particles travel by a speed close to the speed of light, it is approximated to the pseudorapidity, η, which is defined in Equation 3.2.

Appendix B

List of MC samples

Process	Generator	Sample number	σ[pb]
$t\bar{t}$, lepton+jets and dilepton	MC@NLO + Herwig	105200	80.2
Single top, t-channel $\mu\nu$	MC@NLO + Herwig	108341	7.2
Single top, t-channel $\tau\nu$	MC@NLO + Herwig	108342	7.1
Single top, s-channel $\mu\nu$	MC@NLO + Herwig	108344	0.47
Single top, s-channel $\tau\nu$	MC@NLO + Herwig	108345	0.47

Table B.1: Monte Carlo samples of SM top production

Process	Generator	Sample Number	σ[pb]
$Z \to \mu\mu$ +0 parton	Alpgen + Herwig	107660	658
$Z \to \mu\mu$ +1 parton	Alpgen + Herwig	107661	133
$Z \to \mu\mu$ +2 partons	Alpgen + Herwig	107662	39.6
$Z \to \mu\mu$ +3 partons	Alpgen + Herwig	107663	11.1
$Z \to \mu\mu$ +4 partons	Alpgen + Herwig	107664	2.8
$Z \to \mu\mu$ +5 partons	Alpgen + Herwig	107665	0.8
$Z \to \tau\tau$ +0 parton	Alpgen + Herwig	107670	657
$Z \to \tau\tau$ +1 parton	Alpgen + Herwig	107671	133
$Z \to \tau\tau$ +2 partons	Alpgen + Herwig	107672	40.4
$Z \to \tau\tau$ +3 partons	Alpgen + Herwig	107673	11.0
$Z \to \tau\tau$ +4 partons	Alpgen + Herwig	107674	2.9
$Z \to \tau\tau$ +5 partons	Alpgen + Herwig	107675	0.7

Table B.2: Monte Carlo samples of Z production

Process	Generator	Sample Number	σ[pb]
WW +0 parton	Alpgen + Herwig	107100	2.0950
WW +1 parton	Alpgen + Herwig	107101	0.9962
WW +2 partons	Alpgen + Herwig	107102	0.4547
WW +3 partons	Alpgen + Herwig	107103	0.1758
WZ +0 parton	Alpgen + Herwig	107104	0.6718
WZ +1 parton	Alpgen + Herwig	107105	0.4138
WZ +2 partons	Alpgen + Herwig	107106	0.2249
WZ +3 partons	Alpgen + Herwig	107107	0.0950
ZZ +0 parton	Alpgen + Herwig	107108	0.5086
ZZ +1 parton	Alpgen + Herwig	107109	0.2342
ZZ +2 partons	Alpgen + Herwig	107110	0.0886
ZZ +3 partons	Alpgen + Herwig	107111	0.0314
$W^{\pm}W^{\pm}$ +2jets	Madgraph + Pythia	119357	0.221

Table B.3: Monte Carlo samples of diboson productions

Process	Generator	Sample Number	σ[pb]
$t\bar{t}W$	Madgraph + Pythia	119353	0.124
$t\bar{t}W$ +jet	Madgraph + Pythia	119354	0.08
$t\bar{t}Z$	Madgraph + Pythia	119355	0.10
$t\bar{t}Z$ +jet	Madgraph + Pythia	119356	0.08
$t\bar{t}WW$	Madgraph + Pythia	119583	0.001

Table B.4: Monte Carlo samples of associated production of vector bosons with a $t\bar{t}$ pair

Appendix C

Cut Flows

cut	$t_L t_L$	$t_R t_R$	$t_L t_R$	$tt\ m_{Z'} = 100$	$tt\ m_{Z'} = 150$	$tt\ m_{Z'} = 200$
Before cuts	3622.66	3637.71	451.46	36.22	75.12	126.84
Trigger	3578.48	3595.14	445.56	35.71	73.91	124.60
Vertex cut	3544.78	3578.28	442.86	35.61	73.74	124.19
# $\mu > 2$	72.95	79.91	10.36	1.32	2.83	4.67
Bad jet clean	68.73	73.99	9.91	1.25	2.71	4.52
E_T^{mis}	46.88	50.11	6.66	0.61	1.39	2.51
# jets > 2	38.93	36.54	5.49	0.42	1.01	1.82
# $\mu = 2$	38.71	36.54	5.49	0.42	1.01	1.82
same-sign	38.71	36.54	5.49	0.42	1.01	1.82
$M_{\mu\mu} > 15$	38.69	36.54	5.47	0.42	1.01	1.82
Z veto	35.44	35.05	5.08	0.38	0.92	1.63
Reco. truth	35.44	35.05	5.08	0.38	0.92	1.63
# b-jets > 1	33.98	33.63	4.80	0.34	0.85	1.45

Table C.1: Cut flows for all signal samples. Estimations from MC are scaled to the integrated luminosity of 2.05 fb^{-1}.

cut	single top	$t\bar{t}$	Z	$ZZ + WZ + W^{-}W^{+}$	$t\bar{t}W/Z/WW + W^{\pm}W^{\pm}$	fake
Before cuts	77225.33	177667.56	20736360.0	15583.11	764.22	746.63
Trigger	77159.94	176983.48	20628064.0	15313.84	761.67	-
Vertex cut	76895.19	176485.86	20243260.0	15067.32	760.48	-
# $\mu > 2$	185.99	1357.29	679037.19	1234.32	5.45	-
Bad jet clean	182.13	1293.49	675242.25	1210.88	5.17	-
E_T^{mis}	81.56	638.21	286.14	189.39	2.80	34.62
# jets > 2	31.36	491.96	125.42	43.54	2.45	32.62
# $\mu = 2$	31.36	491.98	125.42	36.47	2.14	-
same-sign	0.00	1.36	0.00	1.90	1.23	5.39
$M_{\mu\mu} > 15$	0.00	1.36	0.00	1.90	1.22	5.39
Z veto	0.00	1.07	0.00	1.79	1.14	1.00
Reco. truth	0.00	0.00	0.00	1.79	1.13	1.00
# b-jets > 1	0.00	0.00	0.00	0.14	0.53	1.00

Table C.2: Cut flows for all background samples. The data-driven sample which is used for fake background is made for dilepton studies and the events in this sample are already passed some of the event selections such as trigger, vertex requirement, muon multiplicity requirement and event cleaning cut, before they enter the sample. For other backgrounds the MC samples are used. Estimations from MC are scaled to the integrated luminosity of 2.05 fb^{-1}.

Bibliography

[1] *ATLAS detector and physics performance: Technical Design Report*. Vol. 1. CERN-LHCC-99-014. Geneva: CERN, 1999.

[2] *ATLAS detector and physics performance: Technical Design Report*. Vol. 2. CERN-LHCC-99-015. Geneva: CERN, 1999.

[3] *ATLAS inner detector: Technical Design Report*. Vol. 1. CERN-LHCC-97-016. Geneva: CERN, 1997.

[4] J. A. Aguilar-Saavedra. 'Effective four-fermion operators in top physics: a roadmap'. In: *Nucl.Phys.B* 843:638-672,2011; (Aug. 2010). eprint: `arXiv/1008.3562/hep-ph`.

[5] J. A. Aguilar-Saavedra and M. Perez-Victoria. 'No like-sign tops at Tevatron: Constraints on extended models and implications for the $t\bar{t}$ asymmetry'. In: *Phys.Lett.B* 701:93-100,2011 (Apr. 2011). eprint: `arXiv/1104.1385/hep-ph`.

[6] J. A. Aguilar-Saavedra et al. *Search for Same-Sign Top Pairs and Fourth Generation Bottom-like Quarks in Same-Sign Dilepton Final States with 1* fb^{-1} *of Data*. Tech. rep. ATL-COM-PHYS-2011-710. Geneva: CERN, 2011. URL: `https://cdsweb.cern.ch/record/1358178/export/hx?ln=en`.

[7] G. Altarelli. 'The Standard Model of Particle Physics'. In: (2007). eprint: `arXiv/0510281/hep-ph`.

[8] S. Ask et al. *Report from the Luminosity Task Force*. Tech. rep. ATL-GEN-PUB-2006-002. CERN, 2006.

[9] K. Becker et al. *Mis-identified lepton backgrounds in top quark pair production studies for EPS 2011 analyses*. Tech. rep. ATL-COM-PHYS-2011-768. Geneva: CERN, 2011. URL: `https://cdsweb.cern.ch/record/1361670`.

[10] Edmond L. Berger et al. 'Color Sextet Scalars in Early LHC Experiments'. In: *Phys.Rev.Lett.* 105:181802,2010 (May 2010). eprint: `arXiv/1005.2622/hep-ph`.

[11] Edmond L. Berger et al. 'Top Quark Forward-Backward Asymmetry and Same-Sign Top Quark Pairs'. In: *Phys.Rev.Lett.* 106:201801,2011 (Jan. 2011). eprint: `arXiv/1101.5625/hep-ph`.

[12] O. S. Bruning et al. *LHC Design Report*. Vol. 1: The LHC main ring. Geneva: CERN, 2004.

[13] O. S. Bruning et al. *LHC Design Report*. Vol. 2: the LHC Infrastructure and General Services. Geneva: CERN, 2004.

[14] A. Canepa et al. *Missing Transverse Energy for Top Physics analyses with early ATLAS data at* $\sqrt{s} = 7\ TeV$. Tech. rep. ATL-PHYS-INT-2010-135. Geneva: CERN, 2010. URL: `https://cdsweb.cern.ch/record/1312953`.

[15] ATLAS Collaboration. *Jet Energy Resolution Provider*. URL: `https://twiki.cern.ch/twiki/bin/viewauth/AtlasProtected/JetEnergyResolutionProvider`.

[16] ATLAS Collaboration. *Pileup Reweighting*. URL: `https://twiki.cern.ch/twiki/bin/viewauth/AtlasProtected/PileupReweighting`.

[17] The ATLAS Collaboration. ‘The ATLAS Experiment at the CERN Large Hadron Collider’. In: *JINST* 3 (2008), S08003. DOI: `10.1088/1748-0221/3/08/S08003`.

[18] The CDF Collaboration. ‘Evidence for a Mass Dependent Forward-Backward Asymmetry in Top Quark Pair Production’. In: *Phys.Rev.D* 83:112003,2011 (Jan. 2011). eprint: `arXiv/1101.0034/hep-ex`.

[19] The CDF Collaboration. *Study of the Top Quark Production Asymmetry and Its Mass and Rapidity Dependence in the Full Run II Tevatron Dataset*. Tech. rep. CDF Note 10807. (Preliminary Results for Winter 2012 Conferences). Fermilab, 2012. URL: `http://www-cdf.fnal.gov/physics/new/top/public_tprop.html`.

[20] Celine Degrande et al. ‘An effective approach to same sign top pair production at the LHC and the forward-backward asymmetry at the Tevatron’. In: *Phys.Lett.B* 703:306-309,2011 (Apr. 2011). eprint: `arXiv/1104.1798/hep-ph`.

[21] ATLAS Flavour Tagging Group. *B-tagging for Analysis in Release 16*. URL: `https://twiki.cern.ch/twiki/bin/viewauth/AtlasProtected/Analysis16`.

[22] ATLAS Jet Missing E_T Group. *Recommendations for jet cleaning for data 2011*. URL: `https://twiki.cern.ch/twiki/bin/viewauth/AtlasProtected/HowToCleanJets2011`.

[23] ATLAS Muon Combined Performance Group. *Guidelines for Analysis in Release 16*. URL: `https://twiki.cern.ch/twiki/bin/viewauth/AtlasProtected/MCPAnalysisGuidelinesRel16`.

[24] ATLAS Muon Combined Performance Group. *MuidMuonCollection*. URL: `https://twiki.cern.ch/twiki/bin/viewauth/AtlasProtected/MuidMuonCollection`.

[25] ATLAS Production Group. *Data Periods*. URL: `https://twiki.cern.ch/twiki/bin/viewauth/AtlasProtected/DataPeriods`.

[26] ATLAS Production Group. *MC10b Production Campaign*. URL: `https://twiki.cern.ch/twiki/bin/viewauth/AtlasProtected/AtlasProductionGroupMC10b`.

[27] ATLAS Top Reconstruction Group. *Jets*. URL: `https://twiki.cern.ch/twiki/bin/viewauth/AtlasProtected/TopCommonObjects2011rel16#Jets`.

[28] ATLAS Top Reconstruction Group. *LAr Hole*. URL: `https://twiki.cern.ch/twiki/bin/viewauth/AtlasProtected/TopETmissLiaison_EPS#LAr_Hole`.

[29] ATLAS Top Reconstruction Group. *Muon efficiency scale factors*. URL: `https://twiki.cern.ch/twiki/bin/viewauth/AtlasProtected/TopCommonScales?rev=54#Muon_efficiency_scale_factors`.

[30] ATLAS Top Reconstruction Group. *Muons*. URL: `https://twiki.cern.ch/twiki/bin/viewauth/AtlasProtected/TopCommonObjects2011rel16#Muons`.

[31] ATLAS Top Reconstruction Group. *Top Systematic Uncertainties for 2011 Release16*. URL: `https://twiki.cern.ch/twiki/bin/viewauth/AtlasProtected/TopSystematicUncertainties2011rel16`.

[32] The Particle Data Group. *Particle Physics Booklet*. 2010.

[33] Top Reconstruction Group. *MultijetJESUncertaintyProvider for Top*. URL: `https://twiki.cern.ch/twiki/bin/viewauth/AtlasProtected/MultijetJESUncertaintyProviderTop`.

[34] M. J. Herrero. 'The Standard Model'. In: (2007). eprint: `arXiv/9812242hep-ph`.

[35] Thomas Junk. 'Confidence Level Computation for Combining Searches with Small Statistics'. In: *Nucl.Instrum.Meth.A* 434:435-443,1999 (1999). eprint: `arXiv/hep-ex/9902006`.

[36] D. H. Perkins. 'Introduction to High Energy Physics'. In: 4^{th} ed. Cambridge University Press, 2000, page 19. ISBN: 0 521 62196 8.

[37] CERN Press Release. *LHC research programme gets underway*. URL: `http://press.web.cern.ch/press/PressReleases/Releases2010/PR07.10E.html`.

[38] CERN Press Release. *LHC to run at 4 TeV per beam in 2012*. URL: `http://press.web.cern.ch/press/PressReleases/Releases2012/PR01.12E.html`.

[39] CERN Press Release. *Two circulating beams bring first collisions in the LHC*. URL: `http://press.web.cern.ch/press/PressReleases/Releases2009/PR17.09E.html`.

[40] Pekka K. Sinervo. 'Definition and Treatment of Systematic Uncertainties in High Energy Physics and Astrophysics'. In: (2003). URL: `https://cdsweb.cern.ch/record/931829`.

[41] Hao Zhang et al. 'Color Sextet Vector Bosons and Same-Sign Top Quark Pairs at the LHC'. In: *Phys.Lett.B* 696:68-73,2011 (Sept. 2010). eprint: `arXiv/1009.5379/hep-ph`.

[42] G. Aad et al. 'Measurement of inclusive jet and dijet cross sections in proton-proton collisions at 7 TeV centre-of-mass energy with the ATLAS detector'. In: *Eur. Phys. J.C71* (2011). eprint: `arXiv/1009.5908/hep-ex`.

List of Figures

List of Tables

Author’s Declaration

I hereby certify that the work presented here was accomplished by myself and without the use of illegitimate means or support, and that no sources and tools were used other than those cited.

Bonn, ························ ························
Date Signature